RSC Medicinal Chemistry

ROYAL SOCIETY OF CHEMISTRY

RESEARCH ARTICLE

View Article Online
View Journal

Cite this: DOI: 10.1039/d5md00628g

2-Oxoindolin-thiazoline hybrids as scaffold-based therapeutics for T2DM-associated cognitive impairment: design, synthesis, *in vitro* and *in silico* studies

Wesam S. Qayed, *[a] Mostafa A. Hassan, [a] Halil Şenol,[b] Parham Taslimi [c] and Tarek Aboul-Fadl [a]

Alzheimer's disease (AD) and type 2 diabetes mellitus (T2DM) are closely linked neurodegenerative and metabolic disorders, sharing overlapping pathological mechanisms. In this study, structure-based drug design combined with molecular hybridization strategies was employed to develop dual-acting compounds targeting both conditions. A series of twenty hybrid molecules, comprising 2-oxoindolin-3-thiosemicarbazones (**3a–i**) and thiazolines (**4a–k**) were successfully synthesized and characterized using spectroscopic techniques and elemental analysis. Biological evaluations demonstrated that compounds **3d** and **3h** exhibit potent inhibitory activity against α-glucosidase (α-Glu) and α-amylase (α-Amy), surpassing the efficacy of acarbose. These findings highlight their promising antidiabetic potential and support further investigation into their therapeutic relevance for AD and T2DM comorbidity (**3d** (α-glucosidase K_i = 41.41 ± 2.53 nM; α-amylase IC_{50} = 1.25 ± 0.02 nM), **3h** (α-glucosidase K_i = 44.19 ± 2.41 nM; α-amylase IC_{50} = 2.87 ± 0.16 nM and **acrabose** (α-glucosidase K_i = 101.20 ± 7.53, α-amylase IC_{50} 9.73 ± 0.20). Furthermore, compounds **3i** and **4i** exhibited significantly higher inhibitory activity against acetylcholinesterase (AChE) and butyrylcholinesterase (BChE) compared to the reference drug tacrine. Notably, compound **4i** demonstrated exceptional multi-enzyme inhibition, with kinetic parameters indicating strong binding affinity: **3i** (AChE K_i = 59.71 ± 2.24 nM; BChE K_i = 8.43 ± 0.97 nM), **4i** (AChE K_i = 53.31 ± 1.74 nM; BChE K_i = 10.72 ± 2.19 nM), and **tacrine** (AChE K_i = 132.35 ± 5.90 nM; BChE K_i = 137.42 ± 4.01 nM). Molecular docking and dynamics simulations corroborated these findings by revealing stable and favorable interactions within the active sites of both enzymes. Additionally, *in silico* ADME profiling indicated desirable pharmacokinetic properties, further supporting the therapeutic potential of these compounds as dual-action agents for the management of Alzheimer's disease and type 2 diabetes mellitus.

Received 18th July 2025,
Accepted 29th October 2025

DOI: 10.1039/d5md00628g

rsc.li/medchem

1. Introduction

The global prevalence of both Alzheimer's disease (AD) and diabetes mellitus (DM) is increasing at an alarming rate. A 2024 meta-analysis reported that individuals with diabetes have a 59% higher risk of developing AD compared to non-diabetic individuals. By 2030, it is estimated that the number of people living with diabetes will reach 643 million, while those affected by Alzheimer's disease will number approximately 74.7 million.[1] Emerging evidence suggests that insulin-based therapeutic strategies may hold promise in slowing the progression of AD or potentially preventing its associated complications. Considering AD as a neurodegenerative manifestation of diabetes opens new avenues for innovative treatment approaches, particularly those integrating antidiabetic agents to mitigate or delay the onset and advancement of Alzheimer's disease.

The precise relationship between Alzheimer's disease (AD) and type 2 diabetes mellitus (T2DM) remains a subject of ongoing investigations. However, evidence suggests that poorly regulated blood glucose levels may increase the risk of developing AD. Due to the significant overlap in pathological mechanisms, AD has been referred to by some researchers as "type 3 diabetes" or "diabetes of the brain".[2,3] This terminology stems from the observing impaired insulin

[a] *Department of Medicinal Chemistry, Faculty of Pharmacy, Assiut University, 71526 Assiut, Egypt. E-mail: Wesam.qayed@aun.edu.eg*
[b] *Department of Pharmaceutical Chemistry, Faculty of Pharmacy, Bezmialem Vakif University, 34093 Fatih, İstanbul, Türkiye*
[c] *Department of Biotechnology, Faculty of Science, Bartin University, 74110 Bartin, Türkiye*

signaling contributes to both the accumulation and toxicity of amyloid-beta (Aβ) precursor protein, as well as to decreased Aβ clearance. Additionally, insulin resistance is linked to cellular energy imbalance, promoting the progression of AD. Several shared pathological pathways, such as disrupted insulin and insulin-like growth factor (IGF) signaling, activation of glycogen synthase kinase 3β (GSK-3β), oxidative stress, inflammation, and neurofibrillary tangle formation, further underscore the connection between these two disorders.[4]

1*H*-Indole-2,3-dione (isatin) has garnered increasing attention as a multifunctional scaffold with significant therapeutic potential. As an endogenous molecule, isatin interacts with specific binding proteins, mediating a variety of biological functions.[5] Advanced techniques such as surface plasmon resonance have revealed that isatin modulates the behavior of intracellular amyloid-binding proteins and affects the stability of protein[4] complexes, offering insight into its protective role against β-amyloid toxicity and its regulatory influence on protein interactions.[6] Pharmacological studies have demonstrated that isatin and its derivatives inhibit AChE and BuChE, suggesting their utility in restoring acetylcholine levels in the brain and treating neurodegenerative disorders like Alzheimer's disease. Furthermore, isatin-based compounds have shown promise in diabetes management by inhibiting α-glucosidase and α-amylase, two key enzymes involved in carbohydrate digestion.[7] Thiosemicarbazones, on the other hand, represent another critical class of bioactive compounds, known for their therapeutic effects across multiple disease domains, including bacterial, fungal, parasitic, viral, and neurodegenerative conditions.[8,9] Their structural resemblance to thioureas makes them valuable intermediates in synthesizing pharmacologically active frameworks.

The thiazoline moiety is also a well-known scaffold in medicinal chemistry and has been used to develop new potential bioactive molecules including the well known anti-diabetic drugs pioglitazone and troglitazone.[10] The proven benefits of thiazolines in AD treatment were also reported.[11]

Pharmacophoric integration is a rational drug design approach that combines multiple pharmacophoric elements from different bioactive compounds into a unified scaffold. This strategy aims to enhance biological activity, improve target selectivity, enable multifunctional mechanisms of action, and minimize adverse effects.

Motivated by our previous results on the differing pharmacological profiles of these compound families, a hybridization strategy to combine their key structural features into a single scaffold was pursued.[12,13] In the current work, design, synthesis, and evaluation of a novel set of 1*H*-indole-2,3-dione-based thiosemicarbazones and their cyclized thiazolidine derivatives were undertaken. The synthesized compounds were tested for inhibitory activity against α-amylase, α-glucosidase, AChE, and BChE, aiming to identify candidates with dual antidiabetic and anti-Alzheimer's activity. Additionally, molecular docking and *in silico* modeling were employed to predict and rationalize their biological activity at the molecular level.

1.1. Rationale of design

Encouraged by the established therapeutic potential of isatin-based molecular hybrids,[14] particularly those incorporating thiosemicarbazones[15] and thiazolines,[12,13] and recognizing the urgent need for dual-acting agents capable of addressing both diabetes and Alzheimer's disease, we designed a novel series of hybrid compounds (Fig. 1). These new entities combine all two pharmacophores within one distinct scaffold, intending to achieve both antidiabetic and anti-Alzheimer activities. These novel entities integrate two pharmacophores, thiazolidinone (as in the antidiabetic agent pioglitazone) and indole (as in the anti-Alzheimer drug donepezil), within a single scaffold, with the goal of achieving dual antidiabetic and anti-Alzheimer activities.

Drug discovery is inherently complex, costly, and time-consuming. To accelerate the development of novel therapeutics, virtual screening (VS) has emerged as a vital computational tool for identifying lead compounds from chemical libraries.[16] VS strategies are broadly categorized into ligand-based methods, such as pharmacophore modeling, QSAR, and similarity searches, and structure-based approaches, including molecular docking, homology modeling, and molecular dynamics (MD), which exploit 3D protein structures to assess protein–ligand interactions. In the current study, the molecular docking was implemented to virtually screen the designed isatin–thiosemicarbazone intermediates (**3a–i**) and cyclized isatin–thiazolidine derivatives (**4a–k**) against four target enzymes: α-amylase (α-Amy), α-glucosidase (α-Glu), acetylcholinesterase (AChE), and butyrylcholinesterase (BChE). Docking results were benchmarked against acarbose for α-Amy and α-Glu, and tacrine for AChE and BChE, to evaluate the inhibitory potential of the proposed compounds.

Based on the docking outcomes, compounds (**3a–i**) and (**4a–k**) fit the active pocket of the targeted proteins with variable docking scores and binding affinities comparable to those of reference drugs (acarbose and tacrine). For acetylcholinesterase (AChE), compound **4i** showed strong binding with three hydrogen bonds (two with Tyr-124 and one with Phe-295) and three π–π stacking interactions involving Trp-286, Phe-338, and Tyr-341(docking score −12.391 kcal mol^{-1}). In contrast, compound **3h**, with the lowest docking score (−6.543 kcal mol^{-1}), formed only a single π–π stacking interaction with Tyr-337, indicating weak binding.

Similarly, for butyrylcholinesterase (BChE), compound **3i** hydrogen-bonded with Trp-82 and Thr-120 with a docking

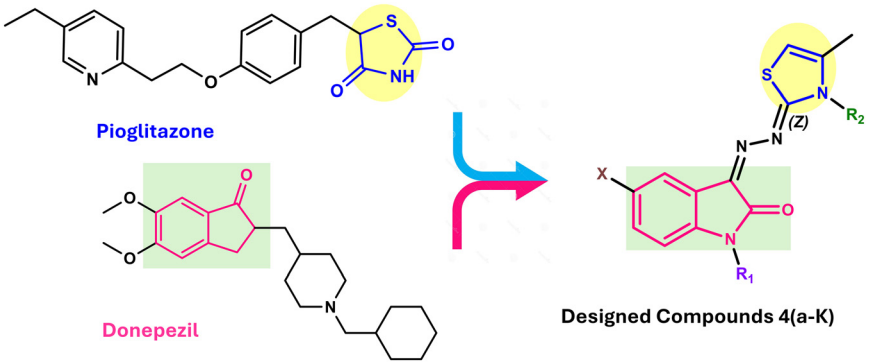

Fig. 1 Proposed structures of designed compounds.

score −10.165 kcal mol^{-1}, whereas **3g**, the least active (docking score −5.925 kcal mol^{-1}), binds through only one hydrogen bond with Glu-197 and one π–π stacking with Tyr-332. In the case of α-amylase, compound **3d** formed four hydrogen bonds with Asp-300 (twice), Asp-197, and Glu-233 (docking score −5.797 kcal mol^{-1}), supporting its strong interaction profile, while compound **3i** exhibited only a single π–π stacking interaction with Trp-59 (docking score −4.768 kcal mol^{-1}). For α-glucosidase, compound **3d** again stood out with two hydrogen bonds involving Asn-202 and Glu-271, compared to **4e**, which formed hydrogen bonds with Asn-333 and Arg-400, likely involving less catalytically relevant residues with docking scores −8.356 and −5.244 kcal mol^{-1}, respectively. Docking patterns and binding interactions are illustrated in the figures provided in the SI (Fig. S1). The promising *in silico* binding affinity of these compounds toward the target proteins suggests their potential as dual-acting modulators, justifying subsequent synthetic efforts and *in vitro* profiling to confirm their mechanism. Additionally, the correlation between docking scores and expected activity underscores the reliability of our computational framework.

Table 1 summarizes docking scores and MM-GBSA Δ*G* binding free energies for the designed compounds **3**(**a**–**i**) and **4**(**a**–**k**), including their *E*/*Z* diastereoisomers, and the target proteins, α-Amy, α-Glu, AChE, and BChE, offering insight into their prospective biological activity. Although the diastereomers revealed similar binding affinities, the result was consistent with earlier reports, where the binding energies of different proteins differed significantly,

Table 1 Docking scores and MM-GBSA Δ*G* binding free energies of synthesized compounds

	Docking Scores (kcal mol^{-1})				MM-GBSA Δ*G* bind. (kcal mol^{-1})			
	AChE	BChE	α-Amy	α-Glu	AChE	BChE	α-Amy	α-Glu
Codes	4EY7	6EP4	5E0F	3WY1	4EY7	6EP4	5E0F	3WY1
3a	−7.274	−6.661	−5.815	−5.988	−31.87	−25.15	−28.55	−25.88
3b	−6.621	−7.002	−5.797	−6.049	−42.90	−33.94	−36.63	−33.31
3c	−8.629	−9.469	−4.905	−7.230	−13.25	−35.35	−41.31	−45.42
3d	−6.766	−8.250	**−8.112**	**−8.356**	−27.97	−29.28	**−41.28**	**−45.09**
3e	−6.717	−7.612	−5.823	−5.452	−20.47	−21.07	−37.99	−32.28
3f	−7.597	−9.334	−5.735	−6.908	−47.82	−33.15	−41.30	−44.08
3g	−7.042	−5.925	−5.623	−5.558	−30.64	−22.32	−33.79	−27.51
3h	−6.543	−6.900	**−6.072**	**−8.008**	−22.04	−33.20	**−31.70**	**−57.39**
3i	**−10.767**	**−10.165**	−4.768	−6.919	**−69.39**	**−51.84**	−35.19	−47.89
4a	−7.960	−7.432	−6.047	−5.501	−54.16	−38.93	−37.08	−28.91
(*E*) **4b**	−8.766	−7.504	−5.033	−6.518	−45.96	−48.34	−31.86	−30.17
(*Z*) **4b**	−6.678	−6.692	−5.009	−6.917	−47.99	−44.75	−41.52	−35.03
(*E*) **4c**	−7.780	−8.251	−5.783	−6.916	−50.29	−53.04	−43.51	−40.62
(*Z*) **4c**	−7.443	−7.728	−5.44	−7.841	−44.96	−38.18	−42.92	−51.49
4d a	−8.677	−8.321	−5.671	−6.774	−30.23	−36.92	−45.76	−32.21
4e	−8.208	−6.285	−6.552	−5.244	−52.74	−34.23	−35.70	−27.64
4f	−7.853	−8.002	−5.159	−6.189	−39.17	−33.97	−42.17	−29.07
4g	−9.268	−8.260	−5.331	−5.417	−40.88	−51.57	−42.04	−25.67
(*E*) **4h**	−8.347	−7.490	−5.657	−5.768	−52.69	−44.79	−41.91	−36.82
(*Z*) **4h**	−7.838	−7.111	−5.015	−7.656	−41.87	−34.30	−44.68	−43.88
4i	**−12.391**	**−9.313**	−5.331	−5.417	**−91.53**	**−71.58**	−42.04	−25.67
4j	−6.861	−7.774	−5.710	−5.528	−40.95	−50.82	−42.60	−19.08
4k	−8.497	−8.438	−4.990	−5.997	−61.84	−46.36	−48.78	−33.29
Acarbose	—	—	−13.205	−7.151	—	—	−67.05	3.96
Tacrine	−7.241	−7.132	—	—	−39.15	−28.97	—	—

suggesting subtle structural influences on ligand–protein interaction dynamics.[12,13]

2. Results and discussions

2.1. Chemistry

Scheme 1 illustrates the synthesis of the novel compounds **4**(**a**–**k**) from the reported intermediates **3**(**a**–**i**).[12,13] Unsubstituted thiazolidine products were obtained from **3a**, **3b**, **3d**, and **3e**, whereas *N*-substituted derivatives resulted from **3g**, **3h**, and **3i**. Interestingly, **3c** and **3f** yielded mixtures of both forms, which were subjected to chromatographic purification to isolate the pure compounds.

The synthesis of compounds **4**(**a**–**k**) extends our previous work in this domain. Earlier analogues featuring *N*-methyl or *N*-ethyl substitutions on the thiazolidine ring limited further modification with chloroacetone. This study focused on the use of unsubstituted thiosemicarbazones, enabling *N*-alkylation with chloroacetone through nucleophilic substitution.

The designed compounds **4**(**a**–**k**) were synthesized following the pathway outlined in Scheme 1. Alkylation of 5-substituted indole-2,3-diones (step A) and the subsequent condensation with thiosemicarbazide (step B) produced the corresponding thiosemicarbazones proceeded efficiently, affording intermediates in high yields of more than 80%. The final cyclisation with chloroacetone (step C) was more sensitive to substituent effects at the 5-position and the N1 substituent, providing the target compounds in slightly lower yields after chromatographic purification and separation. Compounds bearing chloro or trifluoromethyl generally formed single diastereomers, except for the chloro derivative with a benzyl substituent at N1, which produced an *E*/*Z* mixture (**4c**). Similarly, the methoxy substituent provided single diastereomers when N1 was H or *n*-Pr, whereas benzyl substitution again led to *E*/*Z* mixtures (**4g**).

All products were obtained as colored solids and fully characterized by ^{1}H and ^{13}C NMR spectroscopy and elemental analysis, confirming the proposed structures. Mixtures of *E*/*Z* isomers were distinguished by characteristic NMR signals such reactions, common in heterocyclic chemistry involving α-haloketones,[17,18] yielded either pure thiazolidines, acetone-substituted derivatives, or mixtures, depending on the substituents and conditions applied. In

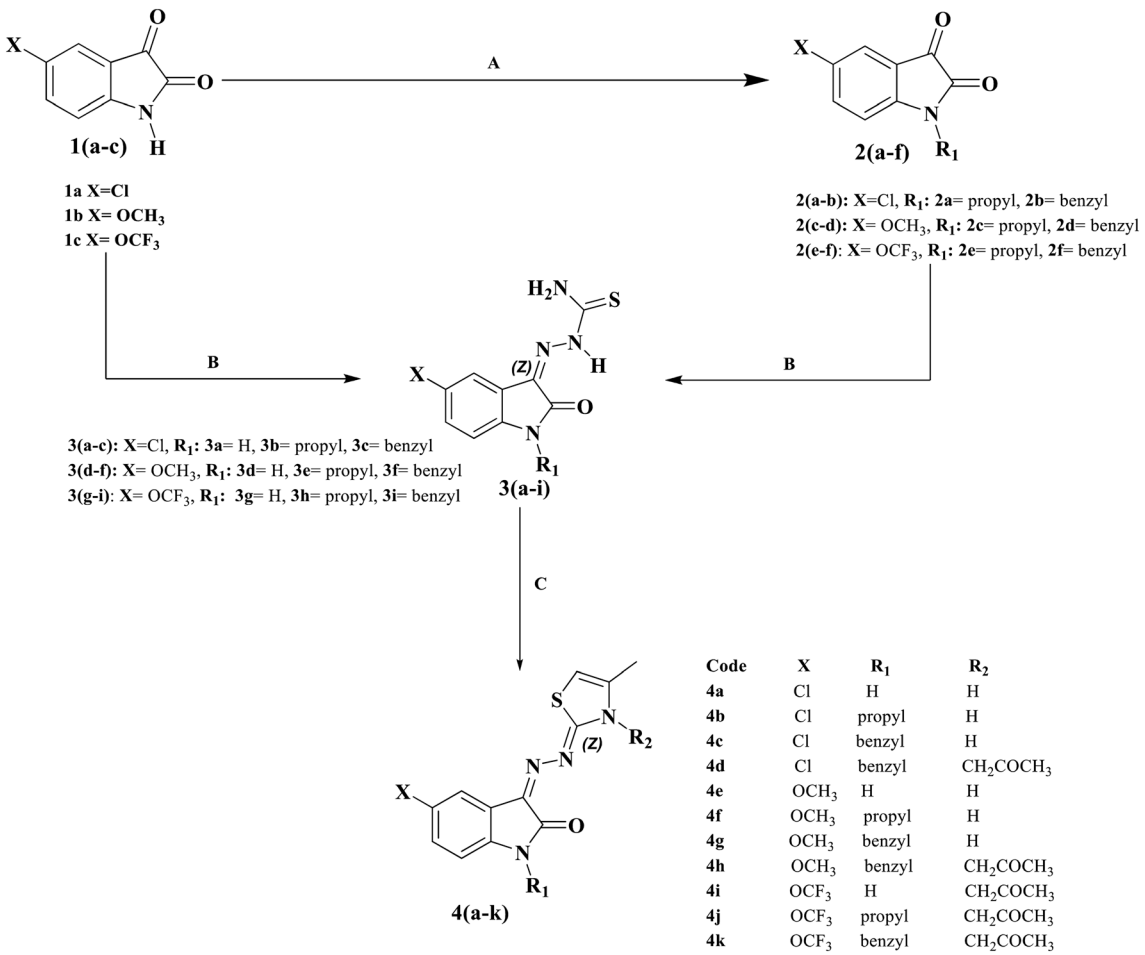

Code	X	R_1	R_2
4a	Cl	H	H
4b	Cl	propyl	H
4c	Cl	benzyl	H
4d	Cl	benzyl	CH_2COCH_3
4e	OCH_3	H	H
4f	OCH_3	propyl	H
4g	OCH_3	benzyl	H
4h	OCH_3	benzyl	CH_2COCH_3
4i	OCF_3	H	CH_2COCH_3
4j	OCF_3	propyl	CH_2COCH_3
4k	OCF_3	benzyl	CH_2COCH_3

Scheme 1 Synthetic pathway for the designed compounds **4**(**a**–**k**); reagents and conditions: (A) 5-substituted indole-2,3-dione (**1a**–**c**) (1 equiv.), R_1-Br (1.1 equiv.), K_2CO_3 (2 equiv.), KI (0.2 equiv.), 30 ml DMF, 80 °C, 45 min, 82–95%; (B) **1**(**a**–**c**) or **2**(**a**–**f**) (1 equiv.) in ethanol, $R_2NHCSNHNH_2$ (1.1 equiv.), reflux, 2 h, 83–96%; (C) **3**(**a**–**i**) (1 equiv.) in ethanol, $ClCH_2COCH_3$ (1.1 equiv.), anhydrous sod. Acetate (2 equiv.), reflux, 24 h, 20–67%.

particular, compounds **4i**, **4j**, and **4k** formed exclusively as acetone-substituted products, suggesting that the presence of a trifluoromethoxy (OCF_3) group may favor this transformation by enhancing nucleophilicity at the thiazolidine nitrogen. A comprehensive investigation of this proposal is planned for a future study.

In certain cases, the reaction favors the formation of stable, unsubstituted thiazolidine rings, as observed in compounds **4a**, **4b**, **4e**, and **4f**. This selectivity is likely driven by stabilizing effects from substituents such as 5-Cl or 5-OCH_3 and small aliphatic groups at $\mathbf{R_1}$, which may reduce N–H reactivity and inhibit alkylation by chloroacetone. Conversely, compounds **3c** and **3f** yielded both acetone-substituted and unsubstituted products (*e.g.*, **4c**, **4d**, **4f**, **4g**), indicating the substituents do not favor a single dominant pathway. In these cases, groups like benzyl at $\mathbf{R_1}$ combined with 5-substituents allow dual product formation, highlighting the nuanced role of electronic and steric effects. The stereoselectivity of the reaction, yielding exclusively *Z*-isomers for compounds **3(a–i)**, is consistent with prior findings. NMR data confirm this configuration, in line with earlier structural reports by our group,[12,13] including those supported by X-ray crystallography.

2.2. Enzyme inhibition studies

The *in vitro* inhibitory properties of the synthesized compounds were investigated against enzymes implicated in diabetes (α-Amy and α-Glu) and neurodegenerative diseases (AChE and BChE). Acarbose (ACR) and tacrine (TAC) were utilized as benchmark inhibitors. The results, including IC_{50} values from inhibition assays and K_i values from enzyme kinetics, are summarized in Table 2.

The IC_{50} values revealed that several compounds exhibited significant inhibitory activity against the target enzymes. Remarkably, compounds **3d**, **3g**, **3h**, **3i**, **4i**, and **4j** displayed the most potent effects. Compound **3d**, in particular, showed outstanding inhibition of α-Glu (IC_{50} = 45.19 ± 0.62 nM, K_i = 41.41 ± 2.53 nM) and α-Amy (IC_{50} = 1.25 ± 0.02 nM), along with appreciable activity against AChE and BChE.

These findings position compound **3d** as a promising multi-target inhibitor. Compounds **3g**, **3h**, **3i**, **4i**, and **4j** revealed comparable potency across several enzymatic targets. Among them, compound **3i** exhibited remarkable selectivity for AChE (70.81 ± 1.19 nM) and BChE (10.87 ± 1.17 nM). Compound **3g** effectively inhibited BChE (19.25 ± 1.32 nM) and α-amylase (3.43 ± 0.67 nM), while 3 h showed balanced inhibition against BChE and α-glucosidase. Compounds **4i** and **4j** delivered the most potent effects, especially against BChE and α-amylase, evidenced by their extremely low IC_{50} values. In addition to the most potent candidates, other synthesized compounds, including **3a–f** and **4a**, **4c–4h**, and **4k**, also showed noteworthy inhibitory effects. Their IC_{50} values ranged from 6–10 nM for α-amylase and 70–100 nM for α-glucosidase. For BChE, inhibition fell between 30–50 nM, while AChE inhibition was observed in the 120–140 nM range. These results highlight the broader potential of the compound series as multi-target enzyme inhibitors. Enzyme kinetic analyses further confirmed that all compounds act through a competitive inhibition mechanism.

Based on the evaluation results, compounds **3d** (α-glucosidase K_i = 41.41 ± 2.53 nM; α-amylase IC_{50} = 1.25 ± 0.02 nM) and **3h** (α-glucosidase K_i = 44.19 ± 2.41 nM; α-amylase IC_{50} = 2.87 ± 0.16 nM) emerged as promising dual-action hit candidates targeting both α-glucosidase and α-amylase. In contrast, compound **3i** (AChE K_i = 59.71 ±

Table 2 *In vitro* enzyme inhibition and enzyme kinetic results of the synthesized compounds

IC_{50} [nM]						K_i [nM]	
Codes	α-Gly	α-Amy	AChE	BChE	α-Gly	AChE	BChE
3a	102.54 ± 0.85	6.39 ± 0.18	100.21 ± 4.13	26.32 ± 0.12	118.35 ± 3.09	91.03 ± 2.07	21.08 ± 1.36
3b	74.11 ± 2.03	7.36 ± 0.49	125.51 ± 0.68	29.52 ± 2.31	60.37 ± 4.48	119.47 ± 1.24	23.71 ± 1.41
3c	82.71 ± 0.42	8.21 ± 0.13	131.08 ± 4.71	41.24 ± 0.34	89.14 ± 4.25	122.61 ± 2.38	32.53 ± 3.28
3d	45.19 ± 0.62	**1.25 ± 0.02**	135.52 ± 0.19	33.04 ± 0.44	**41.41 ± 2.53**	131.74 ± 1.29	27.51 ± 2.80
3e	90.27 ± 2.66	8.55 ± 0.21	136.93 ± 3.28	44.29 ± 2.19	85.09 ± 2.24	132.59 ± 3.32	41.17 ± 3.38
3f	79.17 ± 2.53	9.18 ± 0.20	137.38 ± 4.91	46.54 ± 0.33	75.52 ± 2.48	130.79 ± 2.46	35.75 ± 2.49
3g	54.32 ± 1.73	3.43 ± 0.67	77.41 ± 1.28	19.25 ± 1.32	60.48 ± 2.70	68.54 ± 5.63	15.38 ± 1.04
3h	46.70 ± 1.51	**2.87 ± 0.16**	82.32 ± 1.35	16.09 ± 1.80	**44.19 ± 2.41**	71.65 ± 4.39	12.94 ± 1.05
3i	63.28 ± 1.70	3.19 ± 0.36	70.81 ± 1.19	10.87 ± 1.17	59.71 ± 2.24	**62.51 ± 5.02**	**8.43 ± 0.97**
4a	79.32 ± 1.29	6.84 ± 0.24	116.07 ± 2.32	35.16 ± 1.41	94.42 ± 5.65	102.23 ± 2.19	30.12 ± 2.54
4b	76.91 ± 1.33	7.97 ± 0.56	128.32 ± 3.05	38.04 ± 1.74	92.28 ± 3.07	120.52 ± 4.41	36.24 ± 3.64
4c	72.63 ± 3.55	9.28 ± 0.27	130.40 ± 1.23	45.41 ± 2.11	79.52 ± 5.46	115.18 ± 4.84	39.62 ± 4.21
4d	88.06 ± 2.22	8.39 ± 0.98	133.64 ± 0.54	43.19 ± 1.25	102.73 ± 2.39	129.34 ± 1.06	37.47 ± 3.73
4e	70.46 ± 2.19	6.92 ± 0.06	138.15 ± 2.39	39.12 ± 1.70	68.35 ± 3.19	134.21 ± 4.07	32.39 ± 1.52
4f	89.30 ± 1.08	7.32 ± 0.35	139.04 ± 1.52	35.41 ± 3.24	86.27 ± 5.36	135.48 ± 3.87	30.29 ± 1.64
4g	91.47 ± 4.14	6.74 ± 1.06	134.21 ± 0.66	43.71 ± 2.98	87.64 ± 1.37	121.03 ± 1.51	40.60 ± 1.56
4h	96.05 ± 0.62	9.36 ± 0.29	139.74 ± 3.12	48.63 ± 2.01	92.20 ± 3.56	136.16 ± 1.29	42.51 ± 3.23
4i	59.03 ± 2.48	4.22 ± 0.32	65.29 ± 2.70	13.48 ± 3.54	52.35 ± 3.66	**53.31 ± 1.74**	**10.72 ± 2.19**
4j	51.09 ± 0.34	5.04 ± 0.37	78.15 ± 0.61	15.34 ± 0.22	48.08 ± 2.38	70.22 ± 2.48	10.81 ± 0.38
4k	69.31 ± 2.19	5.75 ± 0.62	89.45 ± 0.22	13.05 ± 0.38	74.82 ± 2.59	81.42 ± 3.33	11.51 ± 1.09
ACR	101.20 ± 7.53	9.73 ± 0.20	—	—	90.42 ± 6.03	—	—
TAC	—	—	137.95 ± 9.04	44.27 ± 3.60	—	132.35 ± 5.91	37.42 ± 4.01

2.24 nM; BChE K_i = 8.43 ± 0.97 nM) and compound **4i** (AChE K_i = 53.31 ± 1.74 nM; BChE K_i = 10.72 ± 2.19 nM) were identified as potent hits for cholinesterase inhibition, showing strong activity against both AChE and BChE.

2.3. Molecular docking studies

Molecular docking studies were carried out to gain insight into the binding behavior and interaction profiles of key compounds with their respective target enzymes. Based on their exceptional inhibitory performance and the lowest IC_{50} and K_i values, compounds **3d**, **3h**, **3i**, and **4i** were selected for computational analysis. The induced fit docking (IFD) method was applied to allow for receptor flexibility and optimize docking accuracy. To quantitatively evaluate binding affinity, MM-GBSA (molecular mechanics/generalized born surface area) calculations were used to estimate the free energy of binding for each ligand–target complex.

Docking simulations identified compounds **3d** and **3h** as top candidates for α-amylase and α-glucosidase inhibition. Compound **3d** exhibited docking scores of −8.112 kcal mol^{-1} (α-Amy) and −8.356 kcal mol^{-1} (α-Glu), while **3h** yielded −6.072 kcal mol^{-1} and −8.008 kcal mol^{-1}, respectively. MM-GBSA analysis revealed favorable binding free energies, particularly for **3h** with −57.39 kcal mol^{-1} against α-Glu. These results are consistent with experimental IC_{50} values, confirming the strong dual-target potential of these compounds for diabetes management.

Targeting cholinesterases, compound **3i** showed superior binding affinity, with docking scores of −10.767 kcal mol^{-1} (AChE) and −10.165 kcal mol^{-1} (BChE), along with MM-GBSA ΔG values of −69.39 and −51.84 kcal mol^{-1}. Similarly, compound **4i** demonstrated exceptional interactions, especially with AChE (−12.391 kcal mol^{-1}; ΔG = −91.53 kcal mol^{-1}). The strong *in vitro* inhibitory activity of both compounds against AChE and BChE underscores their potential as dual-action neuroprotective agents, reinforcing their development as therapeutic candidates for Alzheimer's disease.

Several other synthesized compounds showed moderate yet meaningful binding affinities. Compound **3c**, for example, achieved docking scores of −4.905 kcal mol^{-1} (α-Amy) and −7.230 kcal mol^{-1} (α-Glu), guaranteed by MM-GBSA values of −41.31 and −45.42 kcal mol^{-1}, respectively. Compound (*E*)-**4c** also performed well against α-glucosidase, with a docking score of −6.916 kcal mol^{-1} and a binding free energy of −40.62 kcal mol^{-1}. For cholinesterase inhibition, tacrine exhibited moderate binding with AChE and BChE (docking scores: −7.241 and −7.132 kcal mol^{-1}; MM-GBSA: −39.15 and −28.97 kcal mol^{-1}). However, compounds **3i** and **4i** demonstrated significantly better docking and free energy profiles, suggesting superior efficacy. Although acarbose showed a strong docking score for α-amylase (−13.205 kcal mol^{-1}), its MM-GBSA value for α-glucosidase (+3.96 kcal mol^{-1}) was weak, indicating poor binding stability. In contrast, compound **3h** exhibited better docking and MM-GBSA results for both enzymes, underscoring its broader and more effective inhibitory profile.

2.3.1. The MM-GBSA energy decomposition analysis. To better understand the interactions between the most effective compounds and the target enzymes (α-Amy, α-Glu, AChE, and BChE), MM-GBSA energy decomposition analysis was conducted. This analysis breaks down the total binding energy into key components, such as electrostatic forces, hydrogen bonds, van der Waals forces, lipophilic interactions, solvation effects, and covalent interactions. The results, shown in Table 3, reveal the main factors responsible for the strong binding affinities observed.

The binding analysis for α-amylase revealed that compound **3d** has a high affinity (ΔG_bind = −41.28 kcal mol^{-1}), predominantly through strong coulombic interactions (−36.35 kcal mol^{-1}), with additional support from van der Waals (−27.00 kcal mol^{-1}) and lipophilic (−9.04 kcal mol^{-1}) forces. In contrast, compound **3h** showed less favorable binding (−31.15 kcal mol^{-1}), where the weaker coulombic component (−7.49 kcal mol^{-1}) was offset by substantial van der Waals (−40.80 kcal mol^{-1}) and lipophilic (−15.01 kcal mol^{-1}) contributions. For α-glucosidase, both compounds showed strong binding, with **3d** yielding a ΔG_bind of −45.09 kcal mol^{-1}, dominated by coulombic (−36.89 kcal mol^{-1}) and van der Waals (−37.32 kcal mol^{-1}) interactions. Compound **3h** surpassed this, exhibiting the highest affinity (−57.39 kcal mol^{-1}), due to exceptional van der Waals (−50.57 kcal mol^{-1}) and solid coulombic (−30.74 kcal mol^{-1}) contributions, pointing to a well-balanced electrostatic and hydrophobic interaction profile.

The binding of compound **3i** to AChE yields a ΔG_bind of −69.39 kcal mol^{-1}, mainly due to van der Waals forces (−45.82 kcal mol^{-1}) and coulombic interactions (−13.11 kcal mol^{-1}), though solvation energy contributes positively (+25.76 kcal mol^{-1}). Comparatively, compound **3b** shows superior affinity to AChE (−91.53 kcal mol^{-1}), with stronger coulombic (−24.52 kcal mol^{-1}) and van der Waals (−65.45 kcal mol^{-1}) contributions, suggesting a more robust interaction profile.

In BChE binding, **3i** exhibits a ΔG_bind of −51.84 kcal mol^{-1}, similarly dominated by van der Waals (−45.09 kcal mol^{-1}) and coulombic (−11.11 kcal mol^{-1}) forces. Compound **3b** again stands out (−71.58 kcal mol^{-1}), with high van der Waals (−65.11 kcal mol^{-1}) and coulombic (−21.25 kcal mol^{-1}) energies, reaffirming the importance of both electrostatic and hydrophobic interactions in its binding efficiency.

Overall, the robust binding of **4i** to AChE and BChE, along with the high affinity of **3h** for α-glucosidase, reflects the dominant influence of coulombic and van der Waals interactions. This suggests that these compounds are well-optimized for selective and potent inhibition of their target enzymes.

2.3.2. Molecular docking ligand protein interaction analysis on α-Glu and α-Amy. Molecular docking studies were performed on α-glucosidase and α-amylase to evaluate

Table 3 MM-GBSA energy decomposition analysis of the most active compounds

Complex	PDB ID	ΔG bind	ΔG bind Coulomb	ΔG bind covalent	ΔG bind Hbond	ΔG bind lipo	ΔG bind solv GB	ΔG bind vdW
3d–α-Amy	5E0F	−41.28	−36.35	−0.03	−3.27	−9.04	34.94	−27.00
3h–α-Amy	5E0F	−31.15	−7.49	9.08	−1.75	−15.01	26.20	−40.80
3d–α-Glu	3WY1	−45.09	−36.89	4.84	−2.74	−12.14	39.65	−37.32
3h–α-Glu	3WY1	−57.39	−30.74	1.41	−0.96	−16.46	40.43	−50.57
3i–AChE	4EY7	−69.39	−13.11	3.91	−1.40	−30.51	25.76	−45.82
4i–AChE	4EY7	−91.53	−24.52	5.32	−1.26	−39.55	43.96	−65.45
3i–BChE	6EP4	−51.84	−11.11	0.91	−1.53	−23.88	33.26	−45.09
4i–BChE	6EP4	−71.58	−21.25	9.07	−0.53	−35.64	50.90	−65.11

the binding interactions of compounds **3d** and **3h**. Their ligand–protein complexes, including 2D interaction maps, 3D binding conformations, and interaction modes, are illustrated in Fig. 2 and 3, respectively. Comparative docking data for the reference drug **acarbose** are provided in the SI (Fig. S2–S5).

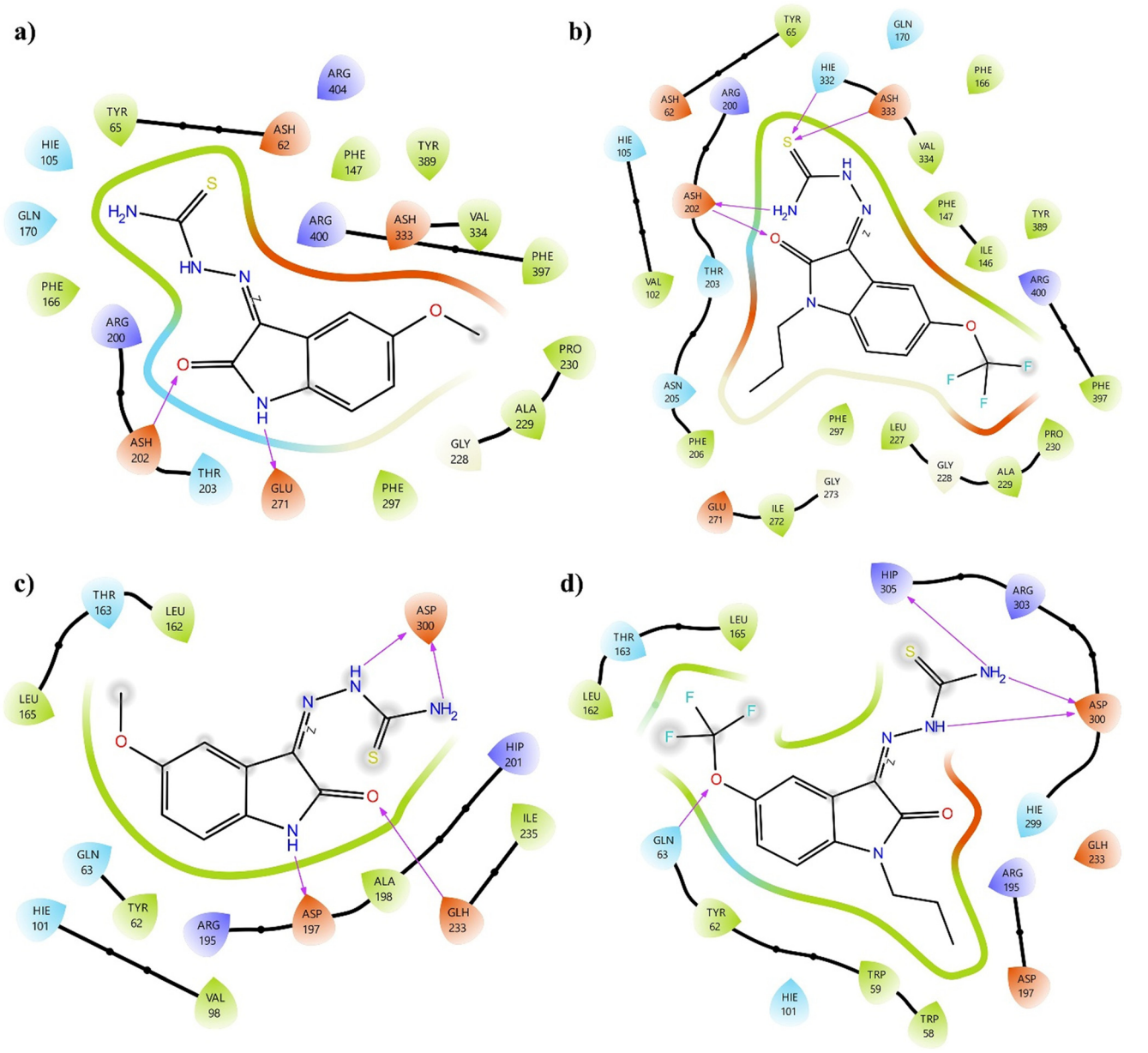

Fig. 2 Molecular docking 2D ligand protein interaction analysis on α-Glu and α-Amy. (a) **3d**–α-Glu complex, (b) **3h**–α-Glu complex, (c) **3d**–α-Amy complex and (d) **3h**–α-Amy complex.

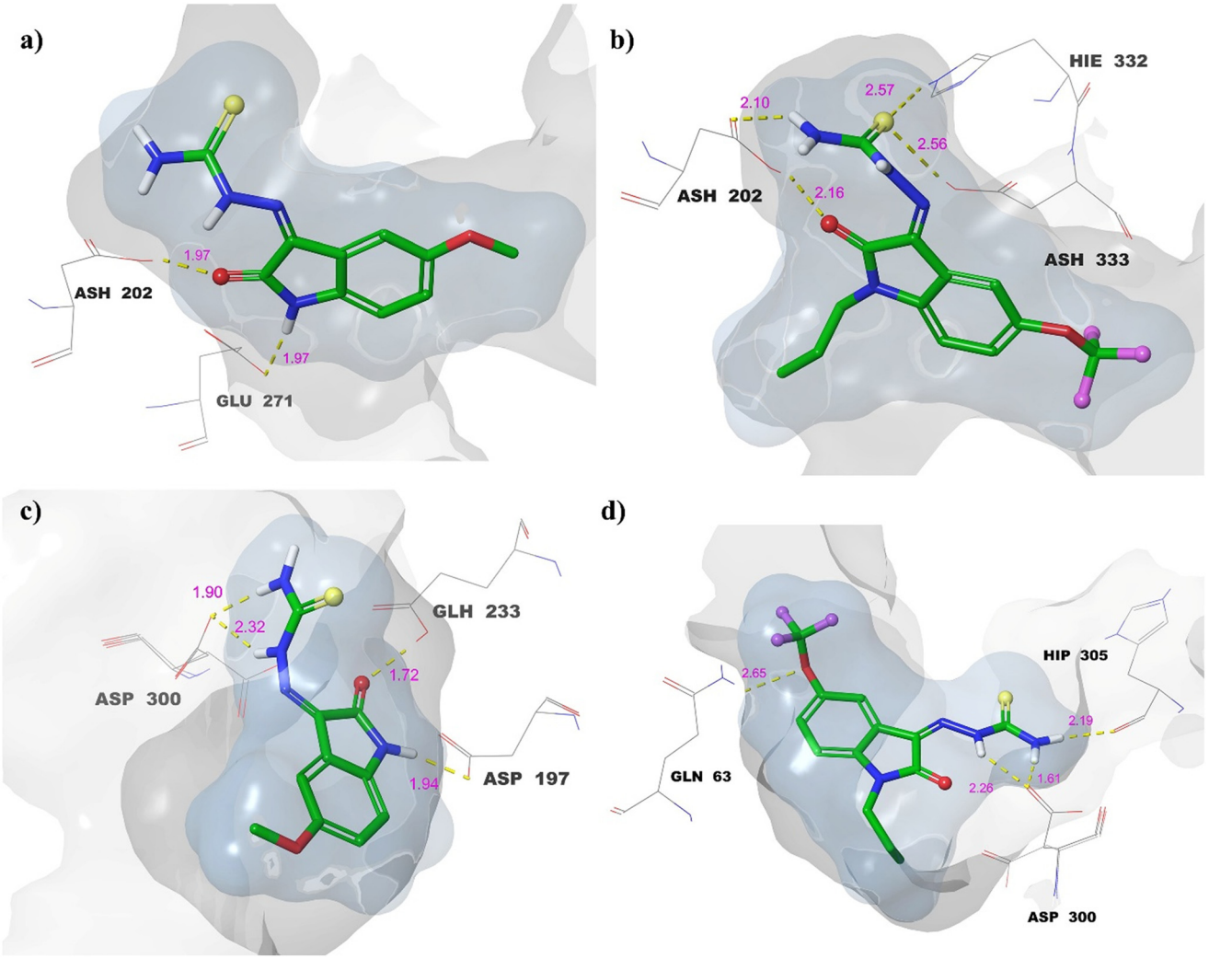

Fig. 3 Molecular docking 3D ligand protein interaction analysis on α-Glu and α-Amy. (a) **3d**–α-Glu complex, (b) **3h**–α-Glu complex, (c) **3d**–α-Amy complex and (d) **3h**–α-Amy complex.

Fig. 2a illustrates the 2D ligand–protein interaction of compound **3d** with α-glucosidase (α-Glu), whereas Fig. 2b shows the interaction of compound **3h** with the same enzyme. Compound **3d** establishes hydrogen bonds with the active site residues **Asp-202** and **Glu-271**. In contrast, compound **3h** forms a total of four hydrogen bonds: two with **Asp-202**, and one each with **His-332** and **Asp-333**. Notably, in both complexes, the ketone oxygen participates in hydrogen bonding with **Asp-202**; however, compound **3h** demonstrates additional interactions through its **urea moiety**, enhancing its binding affinity.

Fig. 2c and d illustrate how compounds **3d** and **3h** interact with α-amylasein 2D binding diagrams. Compound **3d** forms four hydrogen bonds: one each with **Asn-197** and **Glu-233**, and two with **Asp-300**. Compound **3h** also forms four hydrogen bonds, including one with **Asp-300**, which is a shared interaction in both ligands. The **thiourea group** plays a key role in binding to **Asp-300** in both cases. Additionally, **3h** forms bonds with **Gln-63** and **His-305**. The IC_{50} values obtained from α-Amy inhibition tests were 1.25 nM for 3d and 2.87 nM for **3h**, emphasizing the importance of hydrogen bonding in enzyme inhibition.

The 3D binding conformations of compounds **3d** and **3h** with α-glucosidase and α-amylase are presented in Fig. 3a–d. Specifically, Fig. 3a and b display their interactions with α-Glu, while Fig. 3c and d illustrate the α-Amy complexes. **Yellow dashed lines** identify hydrogen bond formations. The **grayish surface** corresponds to the protein binding site, and the **bluish surface** delineates the ligand's spatial fit. Enhanced overlap between these surfaces suggests a more favorable ligand orientation and stronger binding affinity.

As shown in Fig. 3a, compound **3d** forms two strong hydrogen bonds with **α-Glu**, both measuring 1.97 Å. In contrast, compound **3h** exhibits slightly longer hydrogen bonds ranging from 2.10 Å to 2.57 Å (Fig. 3b). For both compounds, the near-complete overlap between ligand and protein binding surfaces indicates excellent fit within **α-Glu**. In Fig. 3c, the **3d–α-Amy** complex forms hydrogen bonds of 1.90 Å, 1.94 Å, and 2.32 Å. However, the **thiourea moiety**

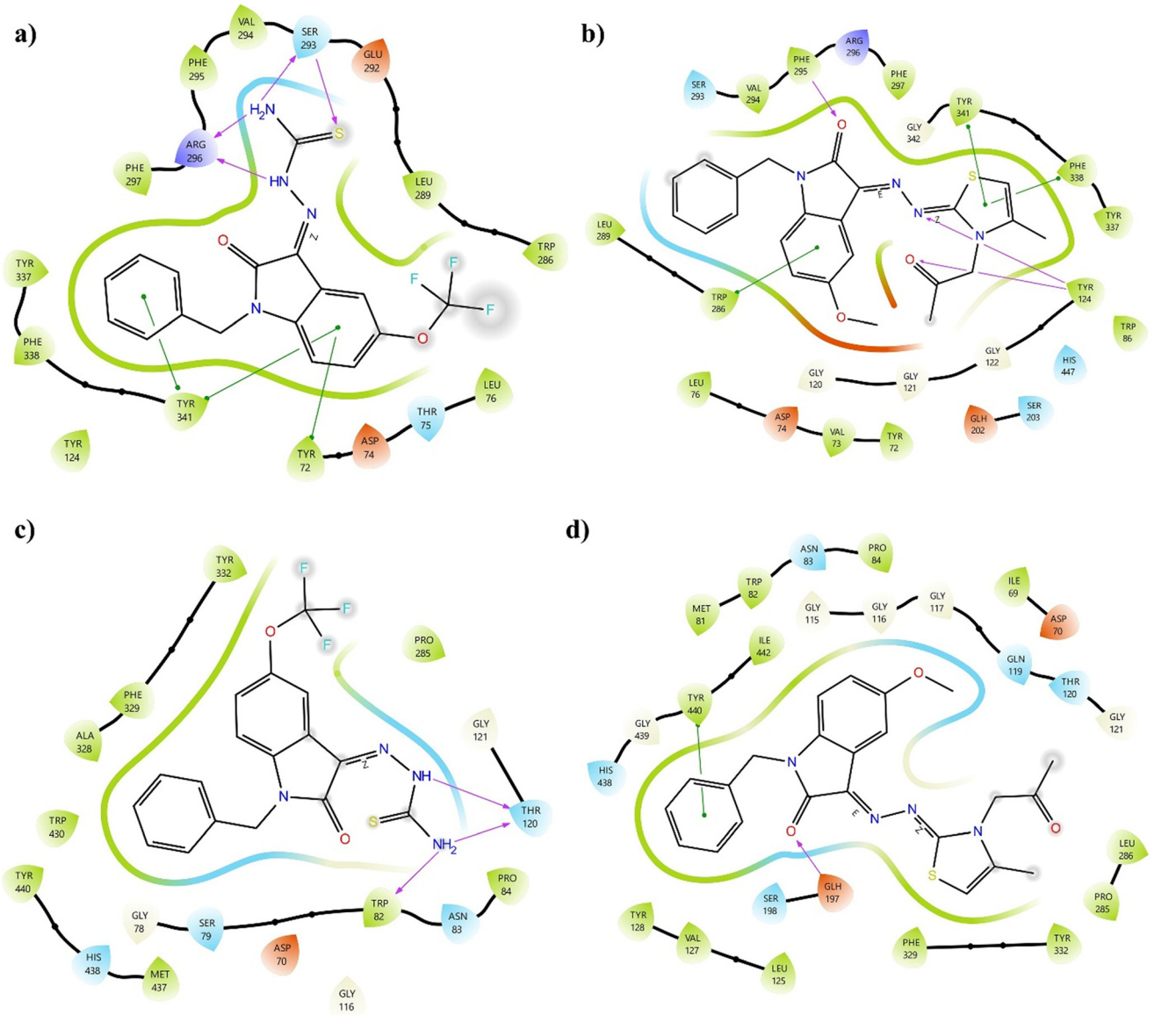

Fig. 4 Molecular docking 2D ligand protein interaction analysis on AChE and BChE. (a) **3i**-AChE complex, (b) **4i**-AChE complex, (c) **3i**-BChE complex, and (d) **4i**-BChE complex.

protrudes outside the binding surface. Similarly, in Fig. 3d, the **3h–α-Amy** complex features hydrogen bonds ranging from 1.61 Å to 2.65 Å, with part of the **thiourea group** and a segment of a **five-membered ring** on the protein lying beyond the binding site. Despite this, both ligands retain inhibitory efficacy, mainly due to hydrogen bonding with the key **Asp-300** residue.

2.3.3. Molecular docking ligand protein interaction analysis on AChE and BChE. As part of the molecular docking studies aimed at Alzheimer's-related targets, compounds **3i** and **4i** were docked into the active sites of **AChE** and **BChE**, and the resulting ligand–protein complexes are visualized *via* 2D and 3D interaction maps and binding models in Fig. 4 and 5. For comparison, the docking results of the reference inhibitor **tacrine** are provided in the SI (Fig. S6–S9).

As shown in Fig. 4a, compound **3i** forms four hydrogen bonds with **Arg-296** and **Ser-293**, and three π–π stacking interactions with **Tyr-341** and **Tyr-72** in its complex with **AChE**. In Fig. 4b, compound **4i** interacts *via* three hydrogen bonds (with **Tyr-124** and **Phe-295**) and three π–π interactions (with **Tyr-341**, **Phe-338**, and **Trp-286**). The strong interaction of **3i** is reflected in a calculated ΔG of −91.53 kcal mol^{-1} and a docking score of −12.391 kcal mol^{-1}, while **4i** also shows considerable binding affinity through its multi-point interactions with the AChE active site.

In Fig. 4c, compound **3i** forms three hydrogen bonds with **Thr-120** and **Trp-82** *via* its thio-urea group in the **BChE** binding pocket. On the other hand, compound **4i** (Fig. 4d) forms a hydrogen bond with **Glu-197** and a π–π stacking interaction with **Tyr-440**. The binding energy (ΔG) for **4i** is −71.58 kcal mol^{-1}, reflecting strong and stable interaction at the BChE

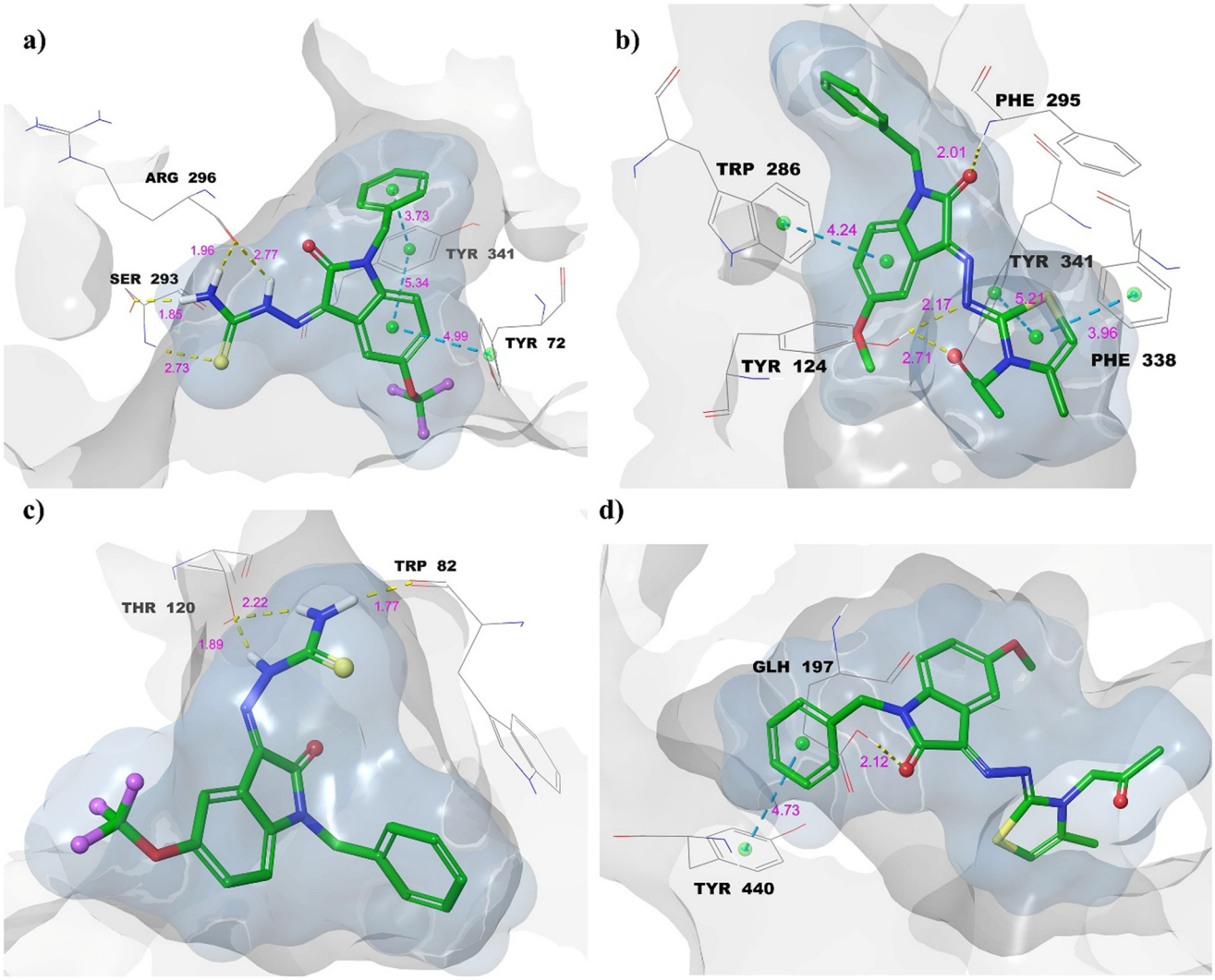

Fig. 5 Molecular docking 3D ligand protein interaction analysis on AChE and BChE. (a) **3i**-AChE complex, (b) **4i**–AChE complex, (c) **3i**–BChE complex, and (d) **4i**-BChE complex.

active site. While both compounds show similar docking scores, the energy profile indicates that compound **4i** achieves a more favorable binding interaction than compound **3i**.

The 3D binding orientations of **3i** and **4i** within **AChE** are illustrated in Fig. 5a and b, respectively. In all representations, hydrogen bonds are shown as yellow dashed lines, while π–π stacking interactions are denoted by turquoise lines. The gray cloud represents the protein surface, and the blue cloud denotes the ligand surface. For the **3i–AChE** complex (Fig. 5a), hydrogen bonds range from 1.85 to 2.77 Å, and π–π stacking occurs at distances between 3.73 and 5.34 Å. The close alignment of the ligand within the protein's surface suggests strong binding. Similarly, in **4i–AChE** (Fig. 5b), hydrogen bond lengths are 2.01, 2.17, and 2.71 Å, and π–π stacking occurs at 3.96 to 5.21 Å, indicating another well-fitting interaction. The 3D binding pose of compound **3i** with BChE (Fig. 5c) shows hydrogen bond interactions with distances between 1.77 and 2.22 Å. In Fig. 5d, the **4i–BChE** complex reveals a hydrogen bond of 2.12 Å and a π–π stacking interaction at 4.73 Å. A portion of the trifluoromethyl group in **3i** and the thiazolidine ring in **4i** extend beyond the protein's surface area, suggesting partial solvent exposure and peripheral positioning within the binding site.

In summary, compound **4i** is the most promising cholinesterase inhibitor identified in this study, supported by its outstanding docking score (−12.391 kcal mol^{-1}) and ΔG bind. (−91.53 kcal mol^{-1}) for **AChE**, and robust binding to **BChE** (docking score: −9.313 kcal mol^{-1}; ΔG: − 71.58 kcal mol^{-1}). This strong affinity is facilitated by interactions with essential residues including Glu-199, Ser-203, His-447 (AChE) and Ser-198, Trp-82, Phe-329 (BChE). Compound **3i** also showed high affinity, particularly with AChE (glide score: −10.767; ΔG: −69.39 kcal mol^{-1}) and BChE (−10.165; ΔG: −51.84 kcal mol^{-1}), involving the same set of key residues. Additionally, compound **3h** presents a compelling case as a dual-target agent, exhibiting moderate inhibition of α-amylase (glide score: −6.072 kcal mol^{-1}; ΔG: −31.15 kcal mol^{-1}) through interactions with Glu-233, Gln-63, and Asp-

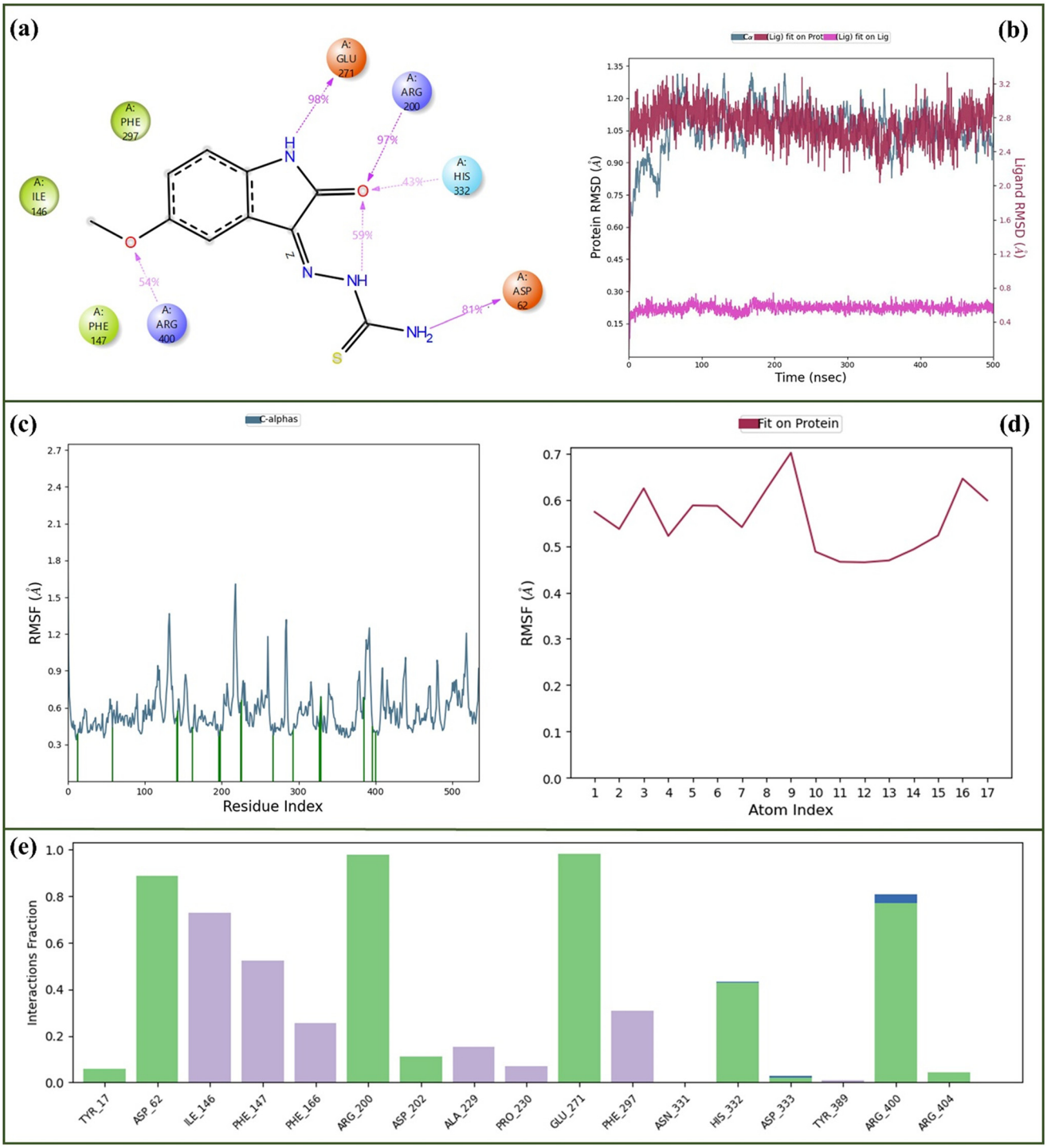

Fig. 6 500 ns MD simulation analysis of the **3d**–α**Glu** complex (a) 2D ligand–protein interactions; (b) RMSD of protein Cα (blue) and ligand (red, pink deviation); (c and d) RMSF of protein and ligand; (e) interaction fractions.

197, thus potentially offering antidiabetic as well as cholinesterase inhibitory effects.

2.4. Molecular dynamics (MD) simulations

Stability and dynamic behavior of the ligand–protein complexes were analyzed *via* 500 ns MD simulations performed on eightsystems: **3d**/**3h**–α-**Amy**, **3d**/**3h**–α-**Glu**, **3i**/**4i**–**AChE**, and **3i**/**4i**–**BChE**. RMSD values tracked overall structural stability, while RMSF values assessed residue-level flexibility throughout the simulation period. Results are presented in Fig. 6–13.

2.4.1. MD simulation analysis on α-Glu. The molecular dynamics (MD) simulation results for **3d**–α**Glu** and

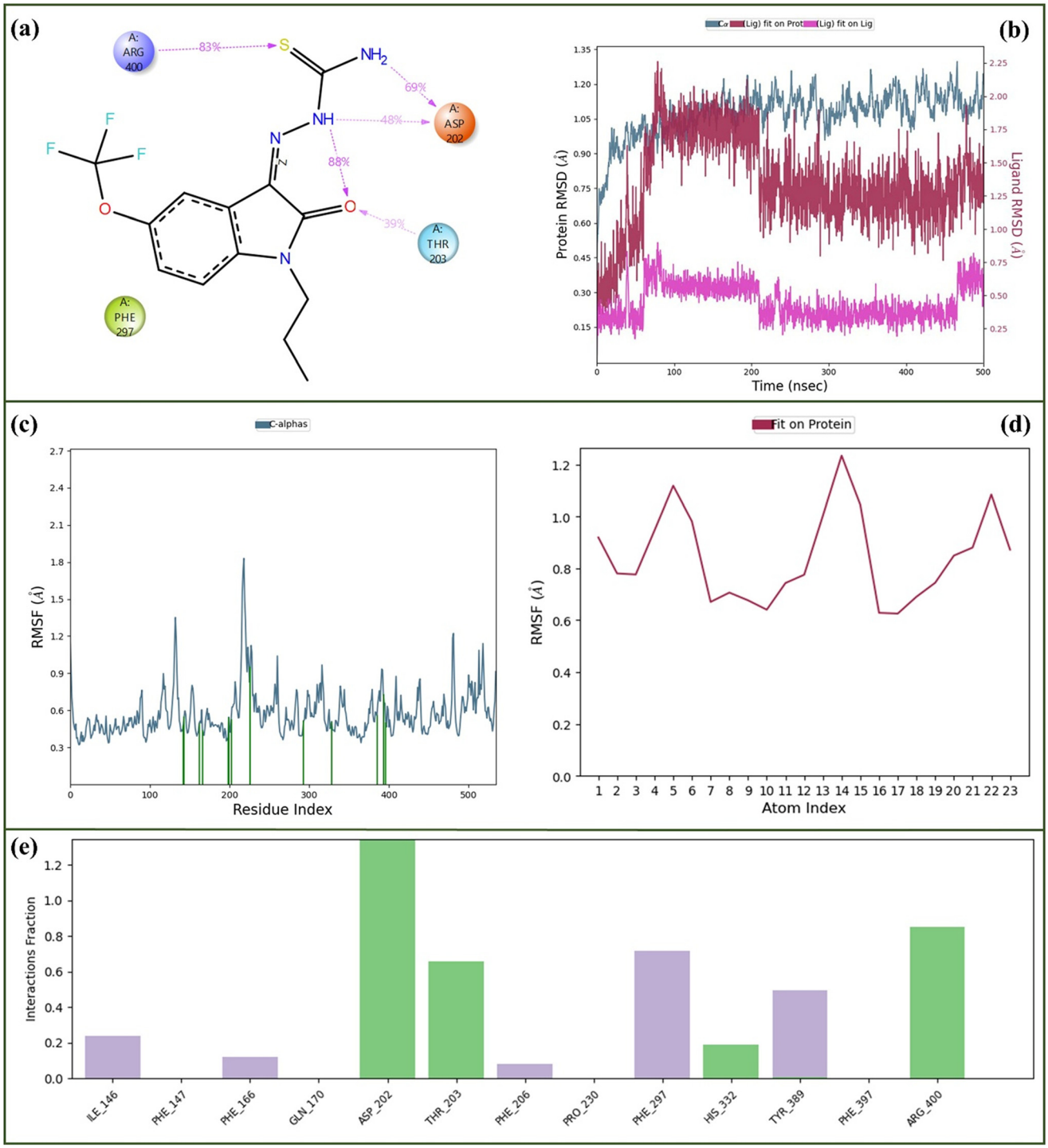

Fig. 7 500 ns MD simulation analysis of the **3h–αGlu** complex (a) 2D ligand–protein interactions; (b) RMSD of protein Cα (blue) and ligand (red, pink deviation); (c and d) RMSF of protein and ligand; (e) interaction fractions.

3h–αGlu over 500 ns are illustrated in Fig. 6 and 7, respectively. Fig. 6a illustrates the 2D ligand–protein interaction map of the **3d–α-Glu** complex throughout the 500 ns trajectory. The carbonyl oxygen of compound **3d** maintained a strong and persistent hydrogen bond with **Arg-200**, while the ring nitrogen interacted consistently with **Glu-271**. Additionally, the thiosemicarbazone amino group formed a stable hydrogen bond with **Asp-62**. The isatin carbonyl was also involved in a hydrogen bond with **His-332**, and the methoxy oxygen interacted with **Arg-400**. An intramolecular hydrogen bond was observed, which persisted for 59% of the simulation time. This intramolecular interaction helped to stabilize the molecular conformation within the binding pocket, thereby

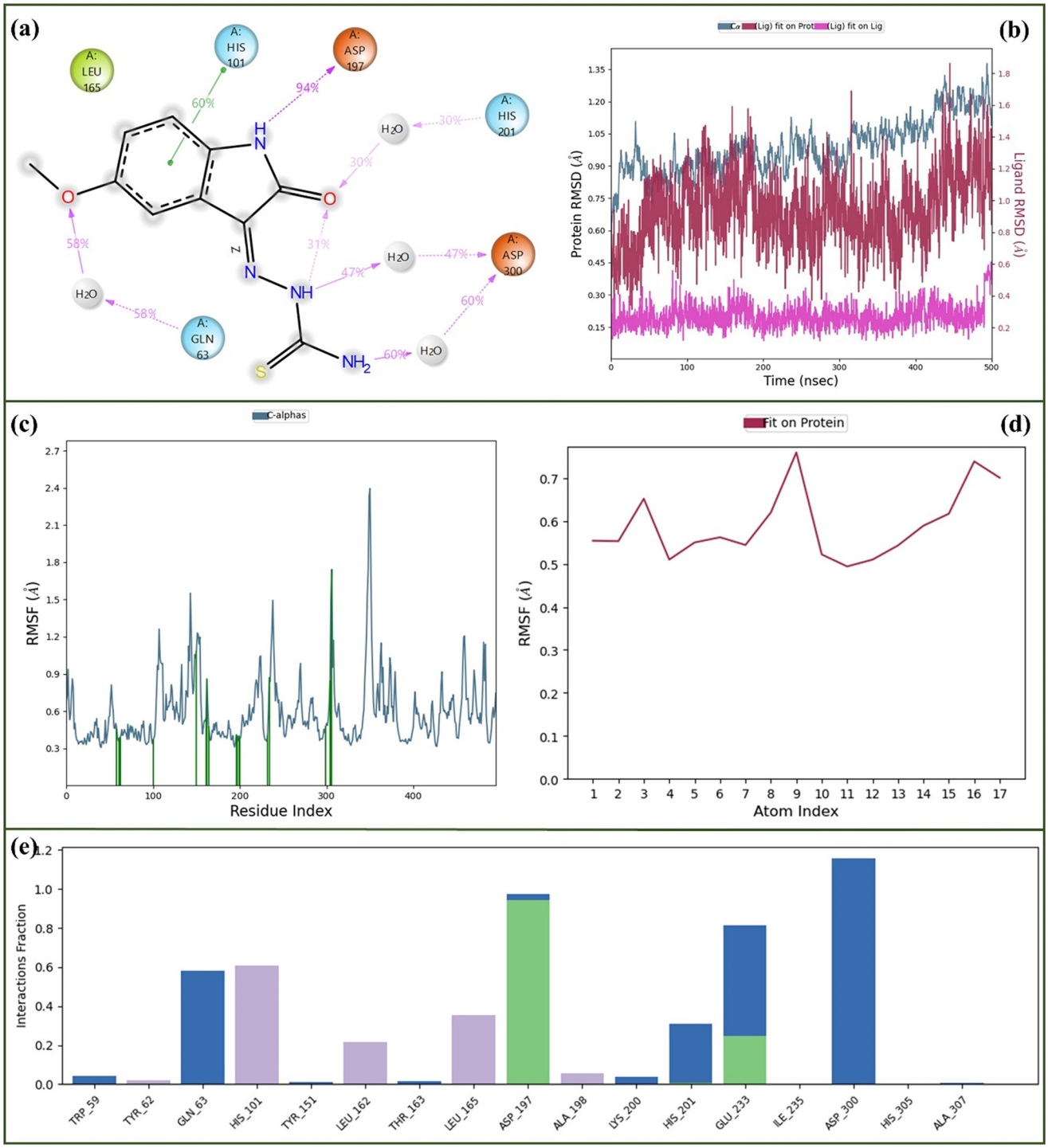

Fig. 8 500 ns MD simulation analysis of the **3d**–αAmy complex (a) 2D ligand–protein interactions; (b) RMSD of protein Cα (blue) and ligand (red, pink deviation); (c and d) RMSF of protein and ligand; (e) interaction fractions.

reducing structural fluctuations and enhancing overall complex stability.

Fig. 6b presents the RMSD plots of protein Cα atoms and ligand atoms. The average RMSD of protein Cα atoms was 1.2 Å (blue), indicating high structural stability, whereas the ligand atoms exhibited an average RMSD of 2.8 Å (red). The ligand's deviation relative to its starting position was only 0.5 Å (pink), suggesting that the binding orientation of **3d** remained well conserved within the active site. Fig. 6c and d show the RMSF values of protein residues and ligand atoms, respectively. The average RMSF of protein Cα atoms was 0.75 Å, while that of the ligand was 0.6 Å. Both values are notably low, reflecting a stable and rigid complex during the 500 ns

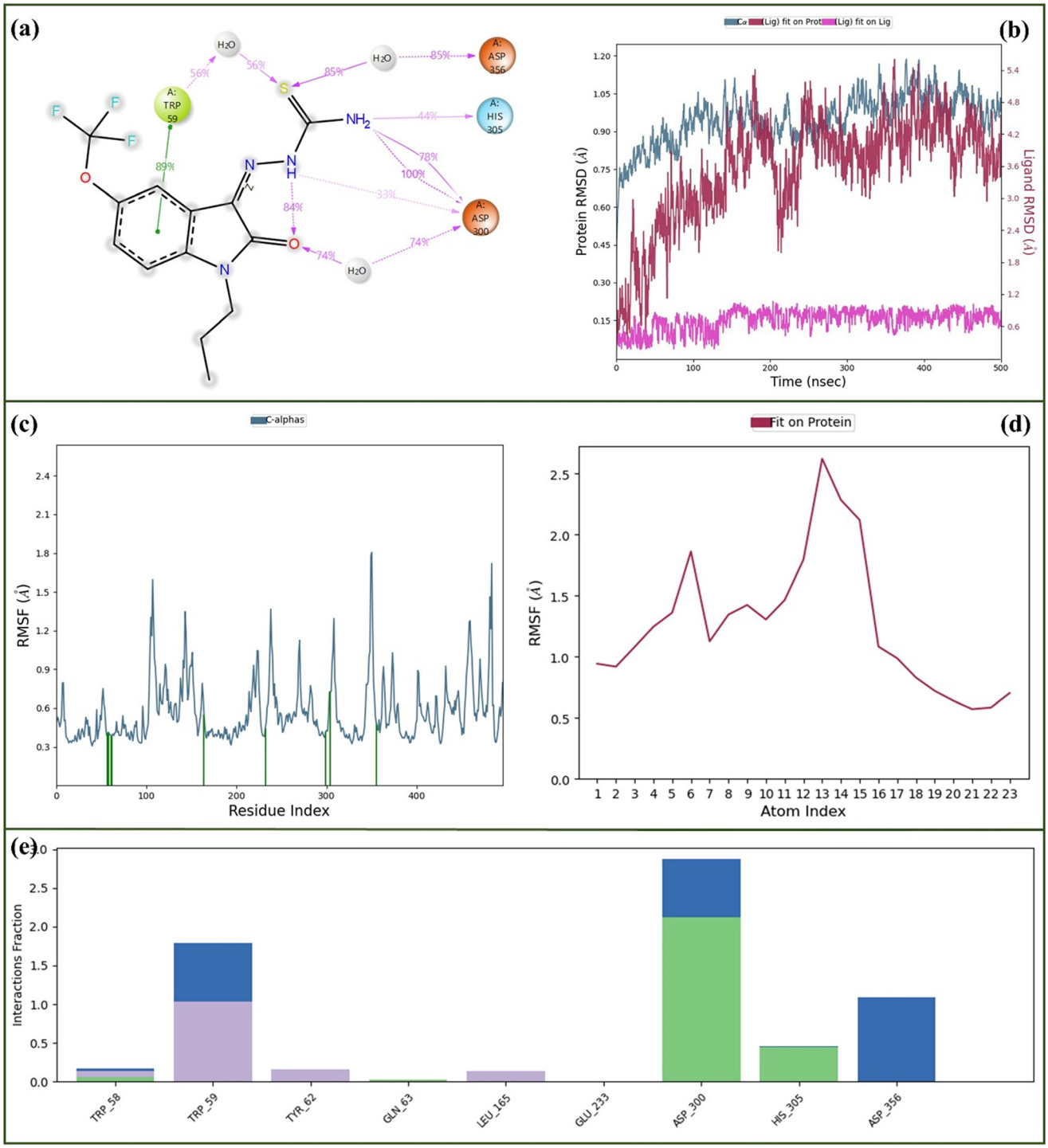

Fig. 9 500 ns MD simulation analysis of the **3h**–**αAmy** complex (a) 2D ligand–protein interactions; (b) RMSD of protein Cα (blue) and ligand (red, pink deviation); (c and d) RMSF of protein and ligand; (e) interaction fractions.

simulation. Fig. 6e displays the fraction of the interaction histogram, where green bars represent hydrogen bonds, blue bars indicate water-mediated hydrogen bonds, and purple bars correspond to hydrophobic interactions. The analysis highlights **Arg-200**, **Glu-271**, **Arg-400**, **Asp-62**, **Ile-146** as the key residues contributing to stable binding interactions with compound **3d**.

Fig. 7a shows the 2D ligand–protein interaction map of the **3h**–**αGlu** complex throughout the 500 ns trajectory. The sulfur atom of **3h** formed a strong hydrogen bond with **Arg-400** (83% of the simulation time). The thiosemicarbazone nitrogens interacted separately with **Asp-202** (69% and 48% of the sim.), and the isatin carbonyl oxygen formed a hydrogen bond with **Thr-203** (39% of the sim.). An

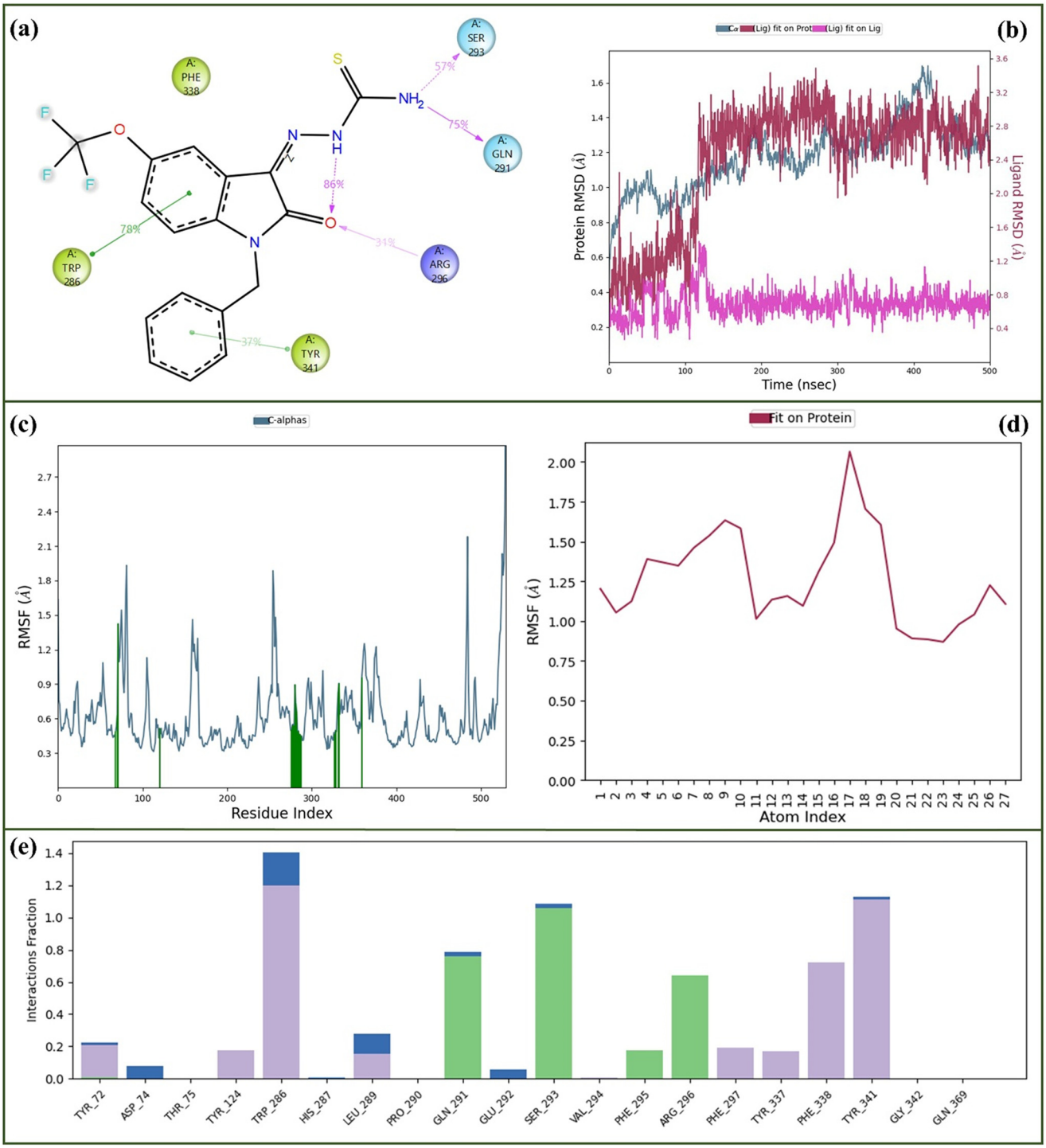

Fig. 10 500 ns MD simulation analysis of the **3i–AChE** complex (a) 2D ligand–protein interactions; (b) RMSD of protein Cα (blue) and ligand (red, pink deviation); (c and d) RMSF of protein and ligand; (e) interaction fractions.

intramolecular hydrogen bond between the carbonyl oxygen and the thiosemicarbazone nitrogen created a five-membered ring, contributing to the conformational stability of the ligand. Fig. 7b presents the RMSD plots of protein Cα atoms and ligand atoms. The average RMSD of protein Cα was 1.2 Å, the ligand RMSD was 1.5 Å, and the ligand's deviation relative to its initial position was 0.5 Å, indicating a stable binding orientation. Fig. 7c and d show RMSF values of protein residues and ligand atoms, respectively. The protein Cα RMSF was 0.9 Å, and the ligand RMSF was 1.0 Å, suggesting moderate flexibility but overall stable interactions. Fig. 7e displays the fraction of the interaction histogram, highlighting hydrogen bonds (green), water-mediated hydrogen bonds (blue), and hydrophobic contacts (purple).

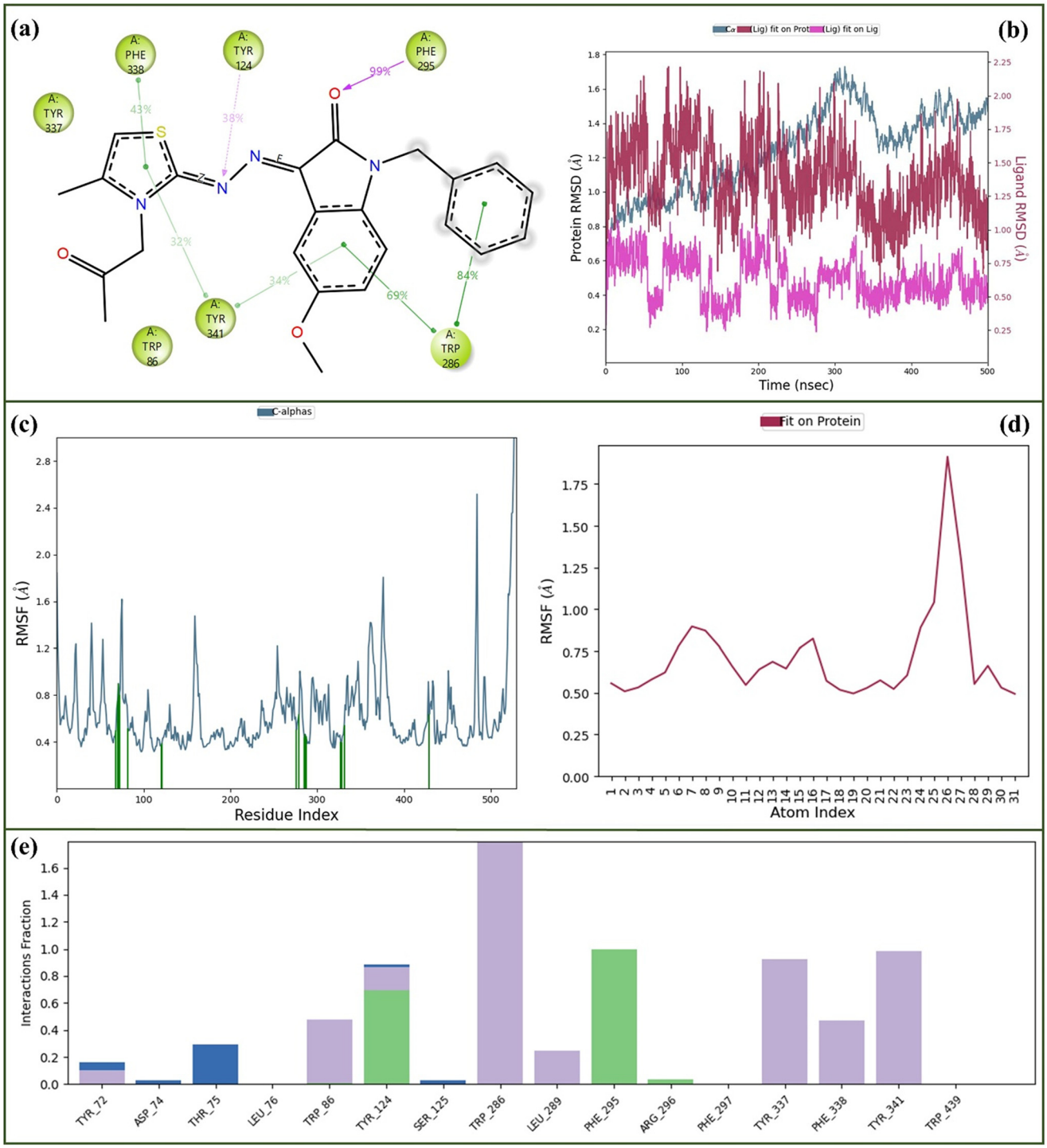

Fig. 11 500 ns MD simulation analysis of the **4i–AChE** complex (a) 2D ligand–protein interactions; (b) RMSD of protein Cα (blue) and ligand (red, pink deviation); (c and d) RMSF of protein and ligand; (e) interaction fractions.

Key residues involved in ligand binding are **Asp-202**, Arg-400, Thr-203, Phe-297, and Tyr-389.

The 500 ns MD simulations indicate that both **3d**- and **3h**-αGlu complexes are stable, with shared key residues **Arg-400** contributing to ligand binding. Compound **3d** forms additional interactions with Arg-200, Glu-271, Asp-62, and His-332, while **3h** interacts uniquely with Asp-202, Thr-203, Phe-297, and Tyr-389. RMSD and RMSF analyses show that **3d** exhibits slightly lower fluctuations and greater rigidity than **3h**, suggesting that **3d–αGlu** is the more stable complex overall. Hydrogen bonds, water-mediated H-bonds, and hydrophobic contacts dominate in both complexes, supporting strong binding affinity.

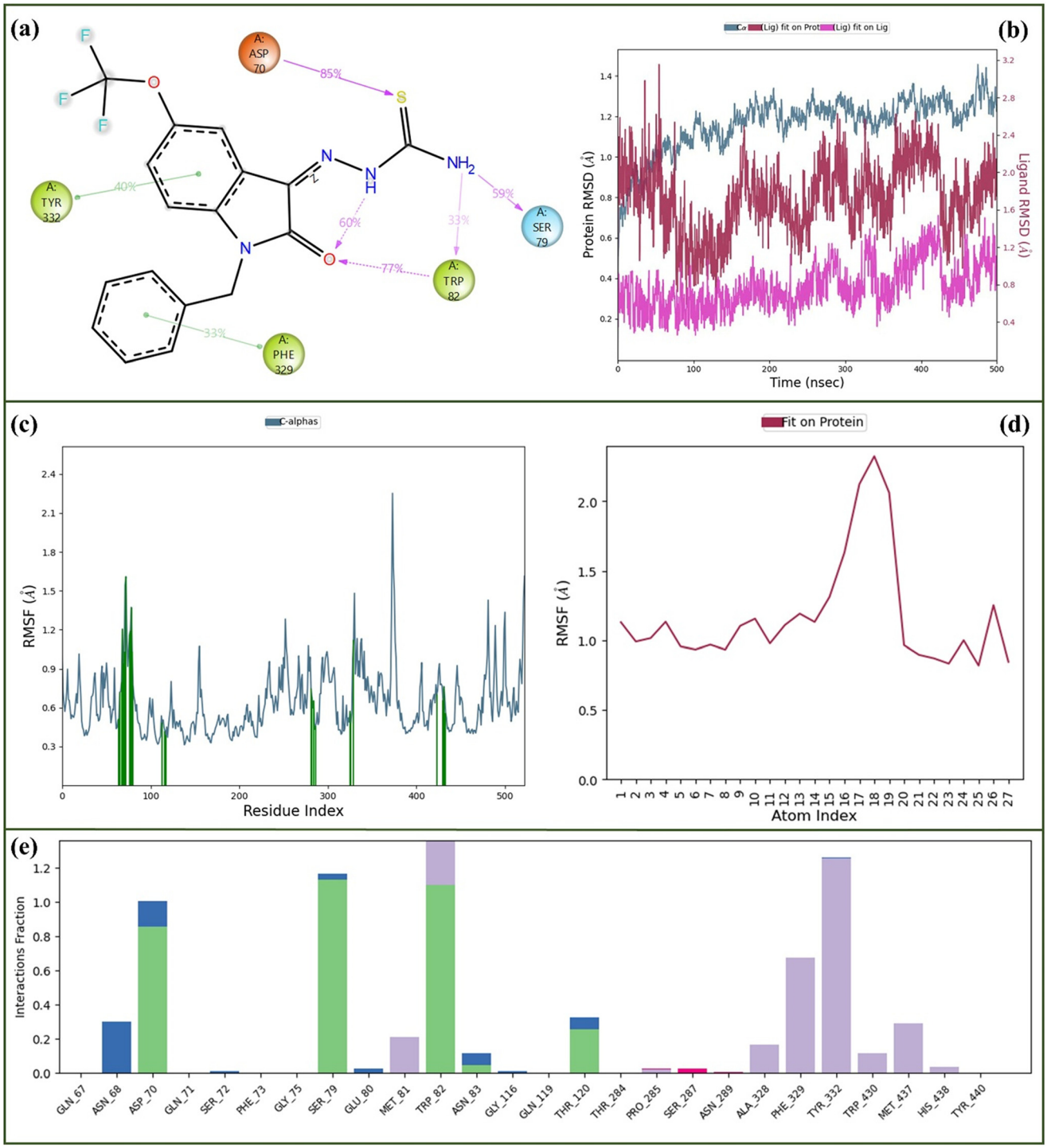

Fig. 12 500 ns MD simulation analysis of the **3i–BChE** complex (a) 2D ligand–protein interactions; (b) RMSD of protein Cα (blue) and ligand (red, pink deviation); (c and d) RMSF of protein and ligand; (e) interaction fractions.

2.4.2. MD simulation analysis on α-Amy. The molecular dynamics (MD) simulation results for **3d–αAmy** and **3h–αAmy** over 500 ns are illustrated in Fig. 8 and 9, respectively. Fig. 8a shows the 2D ligand–protein interaction map of the **3d–αAmy** complex over 500 ns. The pyrrole nitrogen forms a strong hydrogen bond with **Asp-197** (94% of the simulation time), while the isatin carbonyl oxygen engages in a water-mediated hydrogen bond with **His-201** (30% of the sim.). The thiosemicarbazone group forms two water-bridged hydrogen bonds with **Asp-300** (47% and 60% of the sim.), and the methoxy oxygen interacts *via* a water-bridged hydrogen bond with **Gln-63**(58% of the sim.). Additionally, the benzene ring forms a π–π stacking interaction with **His-101** (60% of the sim.). Fig. 8b presents RMSD plots of protein Cα and ligand

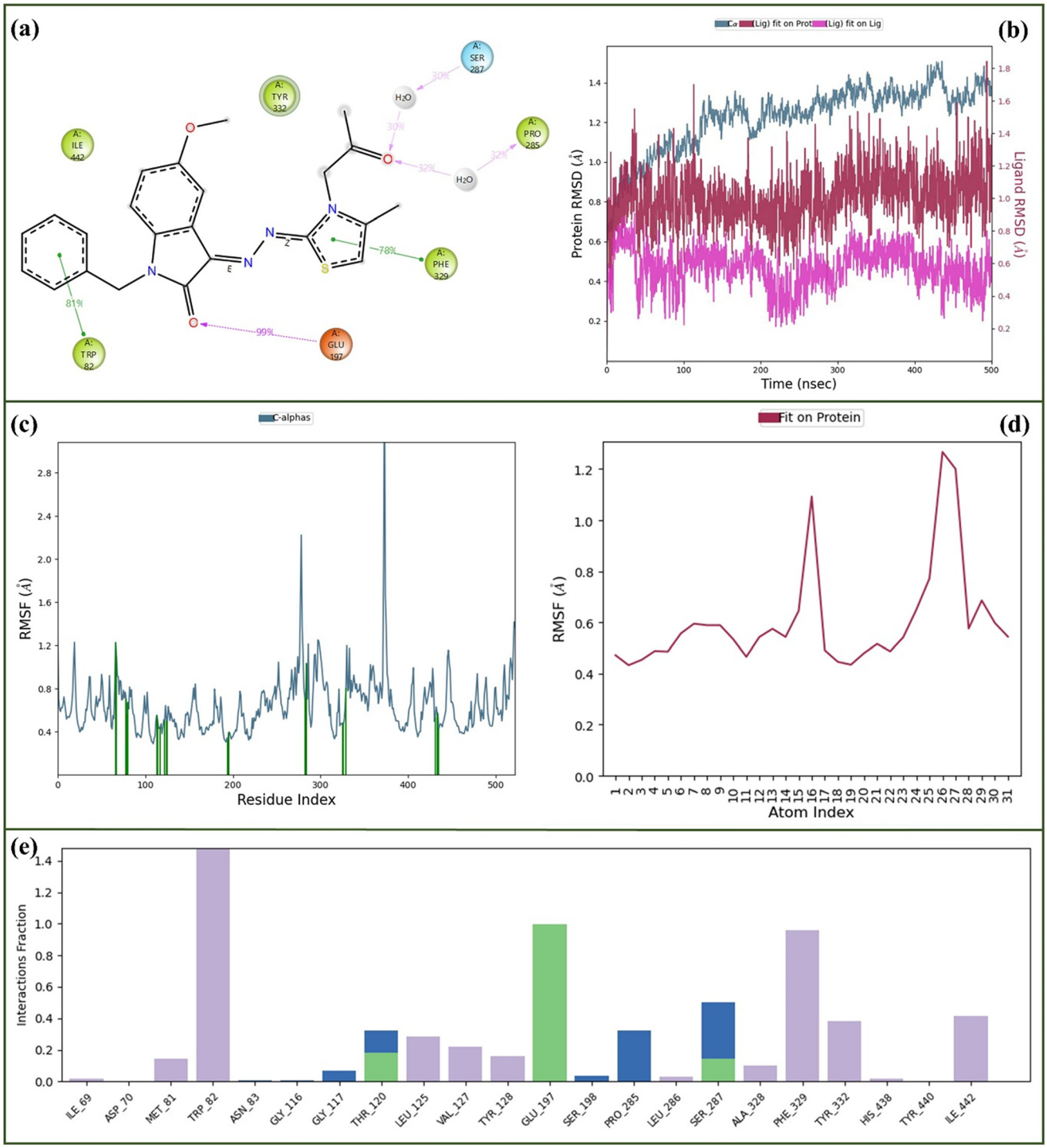

Fig. 13 500 ns MD simulation analysis of the **4i–BChE** complex (a) 2D ligand–protein interactions; (b) RMSD of protein Cα (blue) and ligand (red, pink deviation); (c and d) RMSF of protein and ligand; (e) interaction fractions.

atoms. The average RMSD of protein Cα was 1.1 Å, the ligand RMSD was 1.0 Å, and the ligand deviation relative to its starting position was 0.3 Å, indicating a highly stable binding orientation. Fig. 8c and d show RMSF values of protein residues and ligand atoms. Protein Cα RMSF was 0.75 Å, and ligand RMSF was 0.6 Å, confirming minimal fluctuations and stable complex formation. Fig. 8e displays the fraction of interaction histogram, the key residues contributing to stable binding are **Asp-300**, **Asp-197**, **Glu-233**, with additional involvement of **Gln-63** and **His-101**.

Fig. 9 depicts the 500 ns MD simulation analysis of **3h**-αAmy complex. Fig. 9a shows that compound **3h** maintained multiple interactions throughout the simulation, supporting complex stability.

In Fig. 9a, the thiosemicarbazone–NH_2 group formed two hydrogen bonds with **Asp-300** (100% and 78% of the simulation time), while an additional H-bond was observed between thiosemicarbazone –HN and **Asp-300** (33% of the sim.) and a water-bridged H-bond between the isatin carbonyl oxygen and **Asp-300** (74% of the sim.). Thus, **Asp-300** emerged as the key anchoring residue. Moreover, the –NH_2 group interacted with **His-405** (44% of the sim.), and the sulfur atom formed water-mediated H-bonds with **Trp-59** (56% of the sim.) and **Asp-357** (85% of the sim.). A strong π–π stacking interaction was also observed between the benzene ring and **Trp-59** (89% of the sim.). Fig. 9b displays RMSD profiles, with average values of 1.1 Å for protein Cα (blue), 3.75 Å for the ligand (red), and 0.7 Å ligand deviation from its starting pose (pink), indicating that the protein backbone remained highly stable throughout the simulation, while the ligand exhibited moderate flexibility within the binding pocket. Fig. 9c and d show average RMSF values of 0.8 Å for protein residues and 1.5 Å for the ligand, indicating low protein fluctuations and moderate ligand flexibility. Fig. 9e highlights three key residues stabilizing the complex: **Asp-300**, **Trp-59**, and **Asp-357**, with Asp-300 being the most dominant.

The α-Amy MD simulations demonstrated that both **3d** and **3h** formed stable complexes with the enzyme. In the **3d–αAmy** complex, stability was supported by persistent H-bonds with Asp-197 and Asp-300, together with π–π stacking involving His-101. In contrast, **3h–αAmy** was dominated by multiple strong and long-lasting interactions with Asp-300, supplemented by π–π stacking and water-mediated H-bonds with Trp-59 and Asp-357. The RMSD and RMSF profiles confirmed high protein backbone stability for both complexes, with **3d** showing tighter ligand stability, while **3h** exhibited greater flexibility but stronger anchoring *via* Asp-300.

For the **diabetic target enzymes**, MD simulations indicate enzyme-specific inhibitor preferences. Compound **3d** formed strong and stable interactions with key residues Arg-200, Glu-271, and Asp-62 in **α-glucosidase**, reflected by low RMSD and RMSF values, making it the more stable and effective inhibitor for this enzyme. Conversely, compound **3h** established multiple high-occupancy hydrogen bonds with Asp-300 and π–π stacking with Trp-59 in **α-amylase**, demonstrating superior anchoring and inhibitory potential compared to **3d**.

2.4.3. MD simulation analysis on AChE. The molecular dynamics (MD) simulation results for **3i–AChE** and **4i–AChE** over 500 ns are illustrated in Fig. 10 and 11 respectively. Fig. 10a shows the 2D ligand–protein interaction map of **3i**. The thiosemicarbazone –NH_2 group forms hydrogen bonds with **Gln-291** (75% of the sim.) and **Ser-293** (57% of the sim.).

An intramolecular hydrogen bond between the thiosemicarbazone –NH and the isatin carbonyl (86% of the sim.) creates a five-membered ring, stabilizing the ligand conformation and reducing fluctuations. The isatin carbonyl also interacts with **Arg-296** (31% of the sim.). π–π stacking interactions occur between the benzene ring and **Trp-286** (78% of the sim.) and between the benzyl ring and **Tyr-341** (37% of the sim.). Fig. 10b presents RMSD plots: protein Cα averages 1.5 Å, ligand RMSD 1.5 Å, and ligand deviation relative to its starting pose is 0.7 Å, indicating overall stable binding. Fig. 10c and d show RMSF values, with protein RMSF 0.9 Å and ligand RMSF 1.5 Å, reflecting moderate ligand flexibility and stable protein backbone. Fig. 10e displays the fraction of interactions, highlighting **Trp-286**, **Ser-293**, and **Tyr-341** as key residues, with additional contributions from **Gln-291**, **Arg-296**, and **Phe-338**.

Fig. 11a shows the 2D ligand–protein interactions of **4i–AChE complex**. Multiple π–π stacking and hydrogen bond interactions stabilize the complex. **Trp-286** interacts with the benzyl ring (84% of the sim.) and isatin ring (69% of the sim.) *via* π–π stacking, while **Tyr-341** forms π–π interactions with the isatin ring (34% of the sim.) and thiazole ring (32% of the sim.). The thiazole ring also stacks with **Phe-338** (43% of the sim.). The isatin carbonyl oxygen forms a strong hydrogen bond with **Phe-295** (99% of the sim.), and the thiosemicarbazone imine nitrogen interacts with **Tyr-124** (38%). Fig. 11b presents RMSD plots: protein Cα averages 1.5 Å, ligand RMSD 1.5 Å, and ligand deviation from its initial position is 0.6 Å, indicating stable binding. Fig. 11c and d show RMSF values, with protein Cα RMSF 0.9 Å and ligand RMSF 1.0 Å, confirming moderate ligand flexibility and stable protein structure. Fig. 11e displays the fraction of interactions, highlighting **Trp-286** as the dominant residue, with notable contributions from **Tyr-124**, **Tyr-337**, and **Tyr-439**.

The 500 ns MD simulations of **3i–AChE** and **4i–AChE** complexes demonstrate stable ligand binding within the enzyme active site. In the **3i–AChE** complex, persistent hydrogen bonds with **Gln-291**, **Ser-293**, and **Arg-296**, along with an intramolecular hydrogen bond forming a five-membered ring, stabilized the ligand conformation. π–π stacking interactions with **Trp-286** and **Tyr-341** further reinforced binding, with moderate ligand flexibility (RMSD 1.5 Å, RMSF 1.5 Å). In contrast, **4i–AChE** showed stronger π–π stacking interactions with **Trp-286**, **Tyr-341**, and **Phe-338**, and a highly stable hydrogen bond with **Phe-295** (99%), while maintaining moderate ligand flexibility (RMSD 1.5 Å, RMSF 1.0 Å). Overall, **4i** exhibits slightly stronger anchoring and more extensive π–π interactions, suggesting superior inhibitory potential against AChE compared to **3i**.

2.4.4. MD simulation analysis on BChE. The molecular dynamics (MD) simulation results for **3i–BChE** and **4i–BChE** over 500 ns are illustrated in Fig. 12 and 13 respectively. Fig. 12a shows the 2D ligand–protein interaction map of **3i–BChE** complex. The thiosemicarbazone sulfur forms a hydrogen bond with **Asp-70** (85%), while the thiosemicarbazone –NH_2 group interacts with **Ser-79** (59%) and **Trp-82** (33%). An additional hydrogen bond occurs between Trp-82 and the carbonyl oxygen (77%). As observed in other complexes, an intramolecular hydrogen bond persists at 60%, stabilizing the ligand conformation. The

benzyl group forms a π–π stacking interaction with **Phe-329** (33%), and the isatin benzene ring interacts with **Tyr-332** (40%).

Fig. 12b presents RMSD profiles: average protein Cα RMSD is 1.2 Å (pale blue), ligand RMSD is 2.0 Å, and ligand deviation from its initial pose is 0.8 Å, indicating stable protein backbone and moderate ligand flexibility. Fig. 12c and d show RMSF values, with protein Cα RMSF 0.9 Å and ligand RMSF 1.5 Å, reflecting low protein fluctuations and moderate ligand mobility. Fig. 12e displays the fraction of interactions, highlighting **Trp-82**, **Ser-79**, **Tyr-332**, and **Asp-70** as key residues stabilizing the complex.

Fig. 13a shows the 2D ligand–protein interactions of **4i-BChE** complex. The benzyl ring forms a π–π stacking interaction with **Trp-82** (81%), while the thiazole ring stacks with **Phe-329** (78%). The isatin carbonyl oxygen forms a strong and persistent hydrogen bond with **Glu-197** (99%). Additionally, the ketone oxygen in the side chain engages in two water-bridged hydrogen bonds with **Ser-287** (30%) and **Pro-285** (32%). Fig. 13b presents RMSD plots: average protein Cα RMSD is 1.4 Å, ligand RMSD is 1.1 Å, and ligand deviation from its initial position is 0.6 Å, indicating stable binding. Fig. 13c and d show RMSF values, with protein Cα RMSF 0.8 Å and ligand RMSF 0.9 Å, reflecting low protein fluctuations and moderate ligand stability. Fig. 13e displays the fraction of interactions, highlighting **Trp-82** as the dominant residue, with notable contributions from **Glu-197** and **Phe-329**.

MD simulations of **3i–BChE** and **4i–BChE** complexes indicate stable ligand binding within the enzyme active site. In the **3i–BChE** complex, persistent hydrogen bonds with **Asp-70**, **Ser-79**, and **Trp-82**, along with an intramolecular hydrogen bond and π–π stacking with **Phe-329** and **Tyr-332**, stabilized the ligand, although moderate ligand flexibility was observed (RMSD 2.0 Å, RMSF 1.5 Å). In contrast, the **4i–BChE** complex exhibited stronger and more permanent interactions, including a hydrogen bond with **Glu-197** (99%) and π–π stacking with **Trp-82** and **Phe-329**, supplemented by water-bridged hydrogen bonds with Ser-287 and Pro-285. Ligand flexibility was lower in **4i** (RMSD 1.1 Å, RMSF 0.9 Å), indicating tighter anchoring. Overall, **4i** demonstrates superior binding stability and interaction profile compared to **3i**, suggesting enhanced inhibitory potential against BChE.

2.5. ADME prediction

Understanding a drug's ADME properties—absorption, distribution, metabolism, and excretion, is fundamental to predicting its performance *in vivo*. Using computational tools to estimate these parameters helps identify promising drug candidates early, saving time and resources. Key features like oral bioavailability, solubility, and the ability to cross the blood–brain barrier are evaluated in silico. The results of these predictions are provided in Table 4.

Tacrine is predicted to have moderate CNS activity (CNS = +1), aligning with its known effects in treating Alzheimer's

Table 4 ADME Prediction of synthesized compounds and reference drugs

Title	CNS	Ro5	Ro3	% HOA	QPPCaco	QPPMDCK	QPlogBB	QPlog$P_{o/w}$	QPlogS	aHB	dHB	MW	RB
3a	−1	0	0	76	238	660	−0.736	1.116	−3.25	5	3	254.69	2
3b	0	0	0	91	624	1868	−0.532	2.392	−4.245	6	2	296.77	4
3c	0	0	0	100	711	2152	−0.496	3.293	−4.903	6	2	344.82	4
3d	−1	0	0	74	238	268	−0.969	0.824	−2.841	6	3	250.28	3
3e	−1	0	0	89	622	756	−0.772	2.022	−3.786	6	2	292.36	5
3f	−1	0	0	95	711	873	−0.736	2.923	−4.618	6	2	340.40	5
3g	−1	0	0	80	238	1243	−0.72	1.716	−3.881	5	3	304.25	4
3h	0	0	0	95	620	3500	−0.507	3.035	−4.92	5	2	346.33	1
3i	0	0	1	100	710	4049	−0.47	3.877	−5.716	5	2	394.37	6
4a	0	0	0	93	720	1476	−0.425	2.495	−4.387	5	2	292.74	6
(*Z*) **4b**	0	0	0	100	720	4155	−0.17	3.802	−5.456	6	1	334.82	3
(*E*) **4b**	0	0	0	100	1800	4097	−0.181	3.764	−5.419	6	1	334.82	3
(*E*) **4c**	0	0	1	100	2073	4771	−0.128	4.671	−6.241	5	1	382.87	3
(*Z*) **4c**	0	0	1	100	1763	3723	−0.222	4.642	−6.283	5	1	382.87	3
4d	0	0	0	100	1516	2320	−0.422	4.263	−4.927	7	0	438.93	5
4e	0	0	0	91	720	599	−0.665	2.135	−3.951	5	2	288.32	2
4f	0	0	0	100	1881	1688	−0.407	3.262	−4.779	6	1	330.40	4
4g	−1	0	0	100	1931	1720	−0.467	3.918	−4.139	8	0	434.51	6
(*E*) **4h**	0	0	0	100	2152	2015	−0.344	4.285	−5.681	6	1	378.45	4
(*Z*) **4h**	0	0	1	100	1798	1537	−0.446	4.232	−5.701	6	1	378.45	4
4i	−1	0	0	100	1931	1720	−0.467	3.918	−4.139	8	0	434.51	6
4j	0	0	1	100	1335	4490	−0.458	4.509	−5.795	7	0	440.44	7
4k	0	1	1	100	1013	4030	−0.515	5.08	−6.109	7	0	488.48	7
TAC*	0	0	0	100	2926	1579	0.039	2.572	−3.095	2	1	198.26	0
ACR*	−2	3	2	0	0.019	0.004	−6.691	−8.624	1.501	38	16	791.75	9

Tac: tacrine, Acr: acarbose, CNS: predicted CNS activity (−2 to +2). Ro5: Lipinski's rule violations. Ro3: Jorgensen's rule violations. % HOA: predicted human oral absorption. QPPCaco: Caco-2 cell permeability. QPPMDCK: MDCK cell permeability. QPlogBB: brain/blood partition coefficient. QPlog$P_{o/w}$: octanol/water partition coefficient. QPlogS: aqueous solubility. aHB: H-bond acceptors. dHB: H-bond donors. MW: molecular weight 130–725.

disease. In contrast, the majority of the synthesized compounds show no CNS activity (CNS = 0), making them more appropriate for peripheral nervous system targets. Most synthesized molecules meet all of Lipinski's rule of five criteria (Ro5 = 0), implying strong potential for oral administration, while tacrine fails one criterion. Jorgensen's rule of three highlights tacrine's poor solubility (Ro3 = 2), whereas most test compounds demonstrate better solubility (Ro3 = 0).

The predicted human oral absorption rates (%HOA) formany synthesized compounds are high (up to 100%), unlike acarbose, which is poorly absorbed (0%) and acts locally. Tacrine shows high permeability (QPPCaco = 2926), and many new compounds also show promising values in this regard. CNS permeability, reflected by QPlogBB, is evident for tacrine, while compounds like 3a, 4a, and 3d show negative values, indicating little to no brain penetration. Tacrine's favorable QPlog$P_{o/w}$ and QPlogS values suggest good lipophilicity and solubility for BBB crossing, while synthesized compounds tend to be more hydrophilic—beneficial for solubility but possibly limiting their membrane permeability. Notably, compounds such as **4a** and **3b** have higher hydrogen bonding capacities, which may enhance solubility while possibly compromising permeability compared to tacrine.

Detailed ADME profiling of the lead compounds—**3d**, **3h**, **3i**, and **4i**—highlights favorable pharmacokinetics with peripheral targeting potential. Compound **3d** displays moderate oral absorption (74%) and permeability (QPPCaco = 238), but limited CNS penetration (QPlogBB = −0.736). While compliant with Lipinski's rules, its bioavailability could be hindered by low solubility (QPlogS = −3.25).

Compound **3h** offers a better pharmacokinetic profile with high oral absorption (95%) and permeability (QPPCaco = 620), and acceptable lipophilicity. However, the QPlogBB of −0.507 implies poor BBB penetration, and its low solubility (QPlogS = −4.92) may restrict formulation. Compound **3i** is particularly notable for its perfect absorption rate and outstanding permeability, both intestinal (QPPCaco = 710) and cellular (QPPMDCK = 4049). Despite this, its low solubility (QPlogS = −5.716) could be problematic. Compound **4i** also excels in absorption (100%) and permeability (QPPCaco = 1931), with minimal CNS access (QPlogBB = −0.467), reinforcing its peripheral activity profile, though solubility (QPlogS = −4.139) remains a concern. Collectively, these compounds exhibit excellent absorption and permeability characteristics suitable for peripheral applications, with solubility emerging as the primary optimization parameter.

3. Experimental section

3.1. General

Melting points were measured without correction using a Stuart melting point apparatus (Stuart Scientific, UK). Nuclear magnetic resonance (NMR) spectra were recorded on a Bruker spectrophotometer operating at 400 MHz for ^{1}H and 100 MHz for ^{13}C. Spectra acquisition was performed at the Faculty of Science, Sohag University, Sohag, Egypt, and the NMR facility at the Faculty of Pharmacy, Mansoura University, Mansoura, Egypt. Chemical shifts (δ) are reported in parts per million (ppm) relative to tetramethylsilane (TMS, 0.05% v/v) as the internal standard. Coupling constants (J) are given in hertz (Hz), and the signal multiplicities are designated as follows: singlet (s), doublet (d), triplet (t), quartet (q), and multiplet (m). Deuterated solvents dimethyl sulfoxide (DMSO-d_6) and chloroform ($CDCl_3$) were used. All compounds were dissolved in DMSO-d_6, except for compound **4i**, which was prepared in $CDCl_3$. Elemental analyses were conducted at the Regional Centre for Mycology and Biotechnology, Al-Azhar University, Cairo, Egypt. High-resolution mass spectrometry (HRMS) spectra were obtained using the electrospray ionization (ESI) technique on a Thermo Fisher Scientific Q Exactive™ Hybrid Quadrupole-Orbitrap™ instrument. HPLC chromatograms were recorded using the waters preparative HPLC and PDA detector.

3.2. Chemistry

The synthesis and characterization of intermediates **3**(**a–i**) have been previously described.[12,13] Mass spectra and HPLC purity of compounds **3d**, **3h** and **3i** were performed.

Compound 3d. ESI-HRMS: formula: $C_{10}H_{10}N_4O_2S$, calculated $[M + H]^+$: 251.06027, found $[M + H]^+$: 251.06127 (deviation: 1.0 ppm); **HPLC-PDA:** λ 254 nm, MeCN : MeOH (1 : 1), Rt: 3.99 min, 95.35%.

Compound 3h. ESI-HRMS: formula: $C_{13}H_{16}N_4O_2S$, calculated $[M + H]^+$: 293.10722, found $[M + H]^+$: 293.10827 (deviation: 1.05 ppm); **HPLC-PDA:** λ 254 nm, MeCN : MeOH (1 : 1), Rt: 3.03 min, 96.98%.

Compound 3i. ESI-HRMS: formula: $C_{17}H_{13}F_3N_4O_2S$, calculated $[M + H]^+$: 395.07896, found $[M + H]^+$: 395.07884 (deviation: 0.12 ppm); **HPLC-PDA:** λ 254 nm, MeCN : MeOH (1 : 1), Rt: 3.85 min, 96.14%.

3.3. General procedure for the synthesis of compounds 4(a–k)

A solution of 2-oxoindolin-3-(*Z*)-thiosemicarbazone derivatives **3**(**a–i**) (1 mmol), chloroacetone (1 mmol), and anhydrous sodium acetate (2 mmol) in ethanol (30 mL) was refluxed for 24 hours. After completion of the reaction, the mixture was poured onto crushed ice, resulting in the precipitation of the product. The solid was collected by filtration, washed, and dried to give orange to red compounds. Purification of the crude products was carried out using recrystallization from ethanol and column chromatography, isolating either pure diastereomers or *E*/*Z* isomeric mixtures using an *n*-hexane/ethyl acetate gradient as the eluent system.

(*E*)-5-Chloro-3-(((*Z*)-4-methylthiazol-2(3*H*)-ylidene) hydrazineylidene)indolin-2-one (4a). Yield: 34%; **MP**: 206–208 °C; color: yellow; **^{1}H NMR** (400 MHz, DMSO-d_6) δ 12.55 (s, 1H, N_9H), 10.48 (s, 1H, N_1H), 8.30 (d, J = 2.5 Hz, 1H, C_4H), 7.25 (dd, J = 8.2, 2.4 Hz, 1H, C_6H), 6.84 (dd, J = 8.1,

2.3 Hz, 1H, C_7H), 6.40 (s, 1H, $C_{11}H$), 2.19 (s, 3H, C=C$\underline{CH_3}$). **^{13}C NMR** (100 MHz, DMSO-d_6) δ 178.87 (C=O), 165.63 (thiazole C=N), 141.05 (indole C=N), 140.29 (C_5), 137.39 (C_4), 128.89 (C_{10}), 125.40 (C_6), 125.21 (C_{7a}), 120.74 (C_{3a}), 110.94 (C_7), 101.71 (C_{11}), 13.73 (C_{10a}). **Elemental analysis**: calculated for $C_{12}H_9ClN_4OS$: C, 49.24; H, 3.10; N, 19.14; S, 10.95. Found: C, 49.05; H, 3.07; N, 19.00; S, 10.92.

(*Z*)-5-Chloro-3-(((*Z*)-4-methylthiazol-2(3*H*)-ylidene) hydrazineylidene)-1-propylindolin-2-one (4b). Yield: 67%; **MP**: 200–203 °C; **color**: brownish yellow; **^{1}H NMR** (400 MHz, DMSO-d_6) δ 13.23 (s, 1H, $N_{12}H$), 7.13 (d, J = 8.6 Hz, 1H, C_4H), 7.08 (d, J = 2.7 Hz, 1H, C_6H), 7.01–6.93 (m, 1H, C_7H), 6.77 (s, 1H, $C_{14}H$), 3.71 (t, J = 7.1 Hz, 2H, $N_1\underline{CH_2}CH_2CH_3$), 2.25 (s, 3H, C=C$\underline{CH_3}$), 1.65 (p, J = 7.3 Hz, 2H, $N_1CH_2\underline{CH_2}CH_3$), 0.90 (t, J = 7.4 Hz, 3H, $N_1CH_2CH_2\underline{CH_3}$). **^{13}C NMR** (100 MHz, DMSO-d_6) δ 177.62 (C=O), 164.18 (thiazole C=N), 154.81 (indole C=N), 137.99 (C_5), 136.14 (C_{13}), 135.52 (C_4), 114.13 (C_6), 113.24 (C_{7a}), 108.60 (C_{3a}), 104.92 (C_7), 101.07 (C_{14}), 40.52 (C_8), 20.61 (C_9), 13.74 (C_{13a}), 11.18 (C_{10}). **Elemental analysis**: calculated for $C_{15}H_{15}ClN_4OS$: C, 53.81; H, 4.52; N, 16.73; S, 9.58. Found: C, 54.03; H, 4.35; N, 16.52; S, 9.41.

(*E*/*Z*)-1-Benzyl-3-(((*Z*)-4-methylthiazol-2(3*H*)-ylidene) hydrazineylidene)-5-chloro-indolin-2-one (4c). Yield: 55%; **MP**: 206–208 °C; **color**: yellow; **^{1}H NMR** (400 MHz, DMSO-d_6) (*E*, 67%): δ 12.76 (s, 1H, $N_{16}H$), 8.36 (d, J = 2.3 Hz, 1H, C_4H), 7.40–7.22 (m, 6H, Ph protons and C_6H), 6.94 (d, J = 2.2 Hz, 1H, C_7H), 6.62 (d, J = 1.4 Hz, 1H, $C_{18}H$), 4.96 (s, 2H, $N_1\underline{CH_2}$–Ph), 2.19 (d, J = 1.3 Hz, 3H, C=C$\underline{CH_3}$). (*Z*, 33%): δ 13.14 (s, 1H, $N_{16}H$), 7.54 (d, J = 2.1 Hz, 1H, C_4H), 7.40–7.22 (m, 6H, Ph protons and C_6H), 7.06 (d, J = 8.3 Hz, 1H, C_7H), 6.81 (s, 1H, $C_{18}H$), 5.02 (s, 2H, $N_1\underline{CH_2}$–Ph), 2.26 (d, J = 1.3 Hz, 3H, C=C$\underline{CH_3}$). **^{13}C NMR** (*E*) (100 MHz, DMSO-d_6) δ 178.64 (C=O), 164.03 (thiazole C=N), 140.20 (indole C=N), 137.68 (C_5), 136.62 (C_4), 129.14 (C_{17}), 128.65 (C_{10}), 128.65 (C_{14}), 128.46 (C_6), 127.18 (C_{11}), 127.18 (C_{13}), 127.12 (C_9), 126.00 (C_{7a}), 125.93 (C_{12}), 125.39 (C_{3a}), 110.09 (C_7), 101.63 (C_{18}), 42.45 (C_8), 13.37 (C_{17a}). **Elemental analysis**: calculated for $C_{19}H_{15}ClN_4OS$: C, 59.61; H, 3.95; N, 14.63; S, 8.37. Found: C, 59.11; H, 3.90; N, 14.33; S, 8.07.

(*E*)-1-Benzyl-3-(((*Z*)-4-methyl-3-(2-oxopropyl)thiazol-2(3*H*)-ylidene)hydrazineylidene)-5-chloro-indolin-2-one (4d). Yield: 50%; **MP**: 206–208 °C; **color**: yellow; **^{1}H NMR** (400 MHz, DMSO-d_6) δ 8.02 (d, J = 2.3 Hz, 1H, C_4H), 7.40–7.22 (m, 6H, Ph protons and C_6H), 6.94 (d, J = 2.2 Hz, 1H, C_7H), 6.62 (d, J = 1.4 Hz, 1H, $C_{18}H$), 5.13 (s, 2H, $N_{16}\underline{CH_2}$), 4.96 (s, 2H, $N_1\underline{CH_2}$–Ph), 2.34 (s, 3H, O=C–$\underline{CH_3}$), 2.21 (d, J = 1.3 Hz, 3H, C=C$\underline{CH_3}$). **^{13}C NMR** (100 MHz, DMSO-d_6) δ 200.82 ($\underline{O{=}CCH_3}$), 176.24 (C=O), 164.15 (thiazole C=N), 140.67 (indole C=N), 140.20 (C_5), 137.48 (C_{17}), 136.62 (C_4), 136.44 (C_6), 128.65 (C_{10}), 128.65 (C_{14}), 127.36 (C_9), 127.18 (C_{11}), 127.18 (C_{13}), 125.13 (C_{7a}), 118.89 (C_{12}), 118.48 (C_{3a}), 110.34 (C_7), 102.13 (C_{18}), 54.77 (C_{19}), 42.45 (C_8), 27.49 (C_{20}), 13.64 (C_{17a}). **Elemental analysis**: calculated for $C_{22}H_{19}ClN_4O_2S$: C, 60.20; H, 4.36; N, 12.76; S, 7.30. Found: C, 60.27; H, 3.92; N, 12.66; S, 6.98.

(*Z*)-5-Methoxy-3-(((*Z*)-4-methylthiazol-2(3*H*)-ylidene) hydrazineylidene)indolin-2-one (4e). Yield: 20%; **MP**: 242–247 °C; **color**: brown; **^{1}H NMR** (400 MHz, DMSO-d_6) δ 13.30 (s, 1H, N_9H), 11.02 (s, 1H, N_1H), 7.04 (d, J = 2.4 Hz, 1H, C_4H), 6.94–6.83 (m, 2H, C_6H and C_7H), 6.75 (s, 1H, $C_{11}H$), 3.77 (s, 3H, OCH_3), 2.24 (d, J = 1.1 Hz, 3H, C=C$\underline{CH_3}$). **^{13}C NMR** (100 MHz, DMSO-d_6) δ 177.21 (C=O), 165.85 (thiazole C=N), 154.43 (indole C=N), 138.97 (C_5), 135.57 (C_4), 134.85 (C_{10}), 118.88 (C_6), 114.73 (C_{7a}), 112.97 (C_{3a}), 109.72 (C_7), 100.88 (C_{11}), 55.62 (C_{5a}), 13.78 (C_{10a}). **Elemental analysis**: calculated for $C_{13}H_{12}N_4O_2S$: C, 54.16; H, 4.20; N, 19.43; S, 11.12. Found: C, 54.00; H, 4.22; N, 19.02; S, 10.99.

(*Z*)-5-Methoxy-3-(((*Z*)-4-methylthiazol-2(3*H*)-ylidene) hydrazineylidene)-1-propylindolin-2-one (4f). Yield: 30%; **MP**: 196–198 °C; **color**: yellow-orange; **^{1}H NMR** (400 MHz, DMSO-d_6) δ 13.23 (s, 1H, $N_{12}H$), 7.13 (d, J = 8.6 Hz, 1H, C_4H), 7.08 (d, J = 2.7 Hz, 1H, C_6H), 7.01–6.93 (m, 1H,C_7H), 6.77 (s, 1H, $C_{14}H$), 3.80 (s, 3H, OCH_3), 3.71 (t, J = 7.1 Hz, 2H, $N_1\underline{CH_2}CH_2CH_3$), 2.25 (s, 3H, C=C$\underline{CH_3}$), 1.65 (p, J = 7.3 Hz, 2H, $N_1CH_2\underline{CH_2}CH_3$), 0.90 (t, J = 7.4 Hz, 3H, $N_1CH_2CH_2\underline{CH_3}$). **^{13}C NMR** (100 MHz, DMSO-d_6) δ 177.62 (C=O), 164.18 (thiazole C=N), 154.81 (indole C=N), 137.99 (C_5), 136.14 (C_{13}), 135.52 (C_4), 114.13 (C_6), 113.24 (C_{7a}), 108.60 (C_{3a}), 104.92 (C_7), 101.07 (C_{14}), 55.70 (C_{5a}), 40.52 (C_8), 20.61 (C_9), 13.74 (C_{13a}), 11.18 (C_{10}). **Elemental analysis**: calculated for $C_{16}H_{18}N_4O_2S$: C, 58.16; H, 5.49; N, 16.96; S, 9.70. Found: C, 58.00; H, 5.35; N, 16.90; S, 9.40.

(*E*/*Z*)-1-Benzyl-3-(((*Z*)-4-methylthiazol-2(3*H*)-ylidene) hydrazineylidene)-5-methoxy-indolin-2-one (4g). Yield: 42%; **MP**: 204–206 °C; **color**: orange; **^{1}H NMR** (400 MHz, DMSO-d_6): (*E*, 50%) δ 13.22 (s, 1H, $N_{16}H$), 8.01 (s, 1H, C_4H), 7.40–7.25 (m, 5H, Ph protons), 7.11 (d, J = 2.2 Hz, 1H, C_6H), 6.81 (d, J = 2.9 Hz, 1H, C_7H), 6.79 (d, J = 1.4 Hz, 1H, $C_{18}H$), 4.99 (s, 2H, $N_1\underline{CH_2}$–Ph), 3.77 (s, 3H, OCH_3), 2.26 (s, 3H, C=C$\underline{CH_3}$). (*Z*, 50%) δ 12.49 (s, 1H, N16H), 7.40–7.25 (m, 6H, Ph protons and C_4H), 6.96 (d, J = 2.2 Hz, 1H, C_6H), 6.81 (d, J = 2.9 Hz, 1H, C_7H), 6.40 (d, J = 1.4 Hz, 1H, $C_{18}H$), 4.92 (s, 2H, $N_1\underline{CH_2}$–Ph), 3.74 (s, 3H, OCH_3), 2.20 (s, 3H, C=C$\underline{CH_3}$). **^{13}C NMR** (*E*) (100 MHz, DMSO-d_6) δ 178.64 (C=O), 164.36 (thiazole C=N), 155.02 (indole C=N), 136.99 (C_5), 135.58 (C_4), 128.72 (C_{17}), 128.61 (C_{10}), 128.61 (C_{14}), 127.58 (C_6), 127.22 (C_{11}), 127.22 (C_{13}), 127.36 (C_9), 127.27 (C_{7a}), 113.96 (C_{12}), 113.17 (C_{3a}), 109.03(C_7), 101.63 (C_{18}), 55.68 (C_{5a}) 42.43(C_8), 13.76 (C_{17a}). **Elemental analysis**: calculated for $C_{20}H_{18}N_4O_2S$: C, 63.47; H, 4.79; N, 14.80; S, 8.47. Found: C, 63.18; H, 4.75; N, 14.78; S, 8.41.

(*Z*)-1-Benzyl-3-(((*Z*)-4-methyl-3-(2-oxopropyl)thiazol-2(3*H*)-ylidene)hydrazineylidene)-5-methoxy-indolin-2-one (4h). Yield: 27%; **MP**: 192–195 °C; **color**: yellow-orange; **^{1}H NMR** (400 MHz, DMSO-d_6) δ 7.69 (d, J = 2.2 Hz, 1H, C_4H), 7.39–7.27 (m, 5H, Ph protons), 7.17 (d, J = 2.2 Hz, 1H, C_6H), 6.94 (d, J = 2.2 Hz, 1H, C_7H), 6.56 (d, J = 1.4 Hz, 1H, $C_{18}H$), 5.09 (s, 2H, $N_{16}\underline{CH_2}$), 4.92 (s, 2H, $N_1\underline{CH_2}$–Ph), 3.75 (s, 3H, OCH_3), 2.28 (s, 3H, C=C$\underline{CH_3}$), 2.16 (s, 3H, O=C–$\underline{CH_3}$). **^{13}C NMR** (100 MHz, DMSO-d_6) (*E*/*Z*) δ 206.55, 201.32, 176.74, 176.07, 164.24, 154.99, 139.46, 137.17, 136.81, 130.22, 128.62, 128.56, 128.37,

127.73, 127.30, 127.16, 126.65, 117.87, 114.96, 113.54, 112.74, 109.40, 109.35, 101.07, 55.56, 54.65, 48.61, 42.44, 30.70, 27.26, 13.36. **Elemental analysis**: calculated for $C_{23}H_{22}N_4O_3S$: C, 63.58; H, 5.10; N, 12.89; S, 7.38. Found: C, 63.48; H, 4.95; N, 12.74; S, 6.93.

(*E*)-3-(((*Z*)-4-Methyl-3-(2-oxopropyl)thiazol-2(3*H*)-ylidene) hydrazineylidene)-5-(trifluoromethoxy)indolin-2-one (4i). Yield: 32%; **MP**: 211–213 °C; **color**: yellowish-brown; **^{1}H NMR** (400 MHz, DMSO-d_6) δ 10.69 (s, 1H, N_1H), 7.91 (d, J = 2.6 Hz, 1H, C_4H), 7.26 (dd, J = 8.6, 2.6 Hz, 1H, C_6H), 6.90 (d, J = 8.4 Hz, 1H, C_7H), 6.59 (d, J = 1.5 Hz, 1H, $C_{11}H$), 5.10 (s, 2H, N_9CH_2), 2.27 (s, 3H, C=CCH_3), 2.18–2.13 (s, 3H, O=C–CH_3). **^{13}C NMR** (100 MHz, DMSO-d_6) δ 201.33 (O=CCH_3), 176.75 (C=O), 166.06 (thiazole C=N), 143.03 (indole C=N), 141.43 (C_5), 139.44 (C_4), 137.79 (C_{10}), 123.50 (C_6), 122.09 (C_{5a}), 119.60 (C_{7a}), 118.82 (C_{3a}), 110.88 (C_7), 101.84 (C_{11}), 55.10 (C_{12}), 27.41 (C_{13}), 13.80 (C_{10a}). Compound **4i**: ESI-HRMS: formula: $C_{23}H_{19}F_3N_4O_3S$, calculated $[M + H]^+$: 489.12082, found $[M + H]^+$: 489.12052 (deviation: 0.30 ppm); HPLC-PDA: λ 254 nm, MeCN : MeOH (1 : 1), Rt: 3.03 min, 97.06%. **Elemental analysis**: calculated for $C_{16}H_{13}F_3N_4O_3S$: C, 48.24; H, 3.29; N, 14.06; S, 8.05. Found: C, 48.01; H, 3.49; N, 13.97; S, 7.86.

(*E*)-3-(((*Z*)-4-Methyl-3-(2-oxopropyl)thiazol-2(3*H*)-ylidene) hydrazineylidene)-1-propyl-5-(trifluoromethoxy)indolin-2-one (4j). Yield: 29%; **MP**: 196–199 °C; **color**: yellowish-brown; **^{1}H NMR** (400 MHz, DMSO-d_6) δ 7.99–7.93 (m, 1H, C_4H), 7.34 (dd, J = 8.2, 2.6 Hz, 1H, C_6H), 7.18 (d, J = 8.5 Hz, 1H, C_7H), 6.61 (d, J = 1.5 Hz, 1H, $C_{14}H$), 5.12 (s, 2H, N_9CH_2), 3.71 (t, J = 7.1 Hz, 2H, $N_1CH_2CH_2CH_3$), 2.28 (s, 3H, C=CCH_3), 2.16 (s, 3H, O=C–CH_3), 1.61 (h, J = 7.2 Hz, 2H, $N_1CH_2CH_2CH_3$), 0.87 (t, J = 7.4 Hz, 3H, $N_1CH_2CH_2CH_3$). **^{13}C NMR** (100 MHz, DMSO-d_6) δ 201.27 (O=CCH_3), 176.98 (C=O), 164.58 (thiazole C=N), 143.35 (indole C=N), 141.85 (C_5), 138.37 (C_6), 137.91 (C_{13}), 123.31 (C_4), 119.50 (C_{5a}), 115.04 (C_{7a}), 118.13 (C_{3a}), 109.85 (C_7), 102.10 (C_{14}), 55.16 (C_{15}), 41.18 (C_8), 27.42 (C_{16}), 20.97 (C_9), 13.80 (C_{13a}), 11.59 (C_{10}). Elemental analysis: calculated for $C_{19}H_{19}F_3N_4O_3S$: C, 51.81; H, 4.35; N, 12.72; S, 7.28. Found: C, 51.54; H, 4.05; N, 12.24; S, 7.06.

(*E*)-1-Benzyl-3-(((*Z*)-4-methyl-3-(2-oxopropyl)thiazol-2(3*H*)-ylidene)hydrazineylidene)-5-(trifluoromethoxy)indolin-2-one (4k). Yield: 40%; **MP**: 232-234 °C; **color**: orange; **^{1}H NMR** (400 MHz, $CDCl_3$) δ 7.94 (s, 1H, C_4H), 7.13–7.32 (m, 5H, Ph protons), 6.94 (d, J = 8.6 Hz, 1H, C_6H), 6.58 (d, J = 8.5 Hz, 1H, C_7H), 6.07 (s, 1H, $C_{18}H$), 4.91 (s, 2H, $N_{16}CH_2$), 4.80 (s, 2H, N_1CH_2–Ph), 2.24 (s, 3H, C=CCH_3), 2.09 (s, 3H, O=C–CH_3). **^{13}C NMR** (100 MHz, DMSO-d_6) δ 201.23 (O=CCH_3), 177.15 (C=O), 164.72 (thiazole C=N), 143.57 (indole C=N), 141.30 (C_5), 138.07 (C_{17}), 138.02 (C_4), 136.90 (C_6), 129.17 (C_{10}), 129.17 (C_{14}), 127.88 (C_9), 127.64 (C_{11}), 127.64 (C_{13}), 123.21 (C_{7a}), 119.46 (C_{5a}), 114.19 (C_{12}), 118.32 (C_{3a}), 110.21 (C_7), 102.35 (C_{18}), 55.22 (C_{19}), 43.01 (C_8), 27.43 (C_{20}), 13.81 (C_{17a}). **Elemental analysis**: calculated for $C_{23}H_{19}F_3N_4O_3S$: C, 56.55; H, 3.92; N, 11.47; S, 6.56. Found: C, 56.09; H, 3.73; N, 11, 26; S, 6.49.

3.4. Enzyme inhibition

3.4.1. AChE and BChE assays. The spectrophotometric approach of Ellman *et al.* (1961)[19] was used to test the inhibitory effect of novel derivatives on AChE and BChE activities. The substrate for this reaction was acetylthiocholine and butyrylcholine iodides, respectively. The AChE/BChE activities were measured using 5,50-dithiobis(2-nitro-benzoic)acid (DTNB, D8130-1G, Sigma-Aldrich, Steinheim, Germany). Furthermore, 100 mL of Tris/HCl buffer (1.0 M, pH 8.0) dissolved in distilled water at various concentrations, 50 mL of AChE/BChE (5.32×10^3 U) solution, and 10 mL of sample solution were combined and incubated for 10 minutes at 25 C. 50 milliliters of DTNB (0.5 μM) was then added. The quantity of enzyme required to hydrolyze 1.0 μmol of ACh and BCh per minute at pH 8.0 and 37 °C into choline and acetate is known as one AChE and BChE units.[20–22]

3.4.2. α-Amylase and α-glucosidase. The inhibitory activities of the novel derivatives against α-glucosidase and α-amylase were assessed by the reported protocols by Tao *et al.* and Xiao *et al.*, respectively.[23,24] For the α-glucosidase assay, the used substrate *p*-nitrophenyl-α-D-glucopyranoside (*p*-NPG) dissolved in a phosphate buffer solution at pH 7.4 and a concentration of 5 mM. To prepare sample dilutions, 5 mg of the synthesized compounds were dissolved in 5 mL of a mixture of ethanol and water. Various dilutions of the samples in phosphate buffer were then prepared to achieve complete enzyme inhibition. For the α-amylase assay, a starch substrate solution was prepared by dissolving 3 g of starch in 150 mL of 0.4 M NaOH and heating it at 98°C for 10 minutes. After cooling the solution and adjusting the pH to 7.0 with 2.0 M HCl, the volume was brought up to 200 μL with water. Next, a mixture consisting of 200 μL of phosphate buffer, 50 μL of the substrate, and 5–200 μL of the sample solution was pre-incubated at 35 °C for 3 minutes for the α-glucosidase assay and 30 minutes for the α-amylase assay. The absorbance readings for the α-glucosidase and α-amylase inhibition assays were measured at 405 nm and 580 nm, respectively. These readings were used to determine the inhibitory activities of the synthesized compounds.[25–27]

3.5. Computational studies

Molecular docking and molecular dynamics (MD) simulations were performed using Schrödinger Molecular Modeling Suite (version 2025-1), employing the Maestro interface (v14.3) and Desmond software (D. E. Shaw Research, 2024-4). Protein and ligand preparation adhered to previously established protocols.[28–30] Ligand structures were processed using the LigPrep module to generate all relevant ionization and tautomeric forms at physiological pH (7.4), followed by geometry optimization using the OPLS4 force field. Protein targets—acetylcholinesterase (AChE, PDB ID: 4EY7), butyrylcholinesterase (BChE, PDB ID: 6EP4), α-glucosidase (α-Glu, PDB ID: 3WY1), and α-amylase (α-Amy, PDB ID: 5E0F)—were retrieved from the Protein Data Bank

and prepared using the Protein Preparation Wizard by adding hydrogens, assigning proper protonation states, and performing minimization to resolve steric clashe[31] Glide XP and induced fit docking (IFD) protocols were applied to evaluate ligand–receptor interactions. For IFD, a grid box of 20 × 20 × 20 Å was centered on the binding pocket, and 20 docking poses per ligand were generated. The highest-scoring conformations were refined based on IFD docking scores. The protocol incorporated receptor flexibility, enabling iterative adjustments of both ligand and protein conformations to reflect a realistic dynamic binding process.[32] Prime MM-GBSA calculations, employing the VSGB solvation model, were performed to estimate the binding free energies of the docked protein–ligand complexes. This method evaluates the energetic favorability of binding by considering electrostatic interactions, van der Waals forces, and solvation effects.[33]

MD simulations were carried out in Desmond using the TIP4P water model for solvation. The system was neutralized with Na^+ and Cl^- ions, and a 10 × 10 × 10 Å simulation box was employed. After energy minimization to resolve initial steric clashes, the system was equilibrated under NPT conditions at 300 K and 1 atm. A production run was then conducted for 100 ns. RMSD analysis of the protein backbone and ligand atoms was performed to assess conformational stability. Additionally, the persistence of key interactions, including hydrogen bonds, hydrophobic contacts, and salt bridges, was examined to evaluate the strength and stability of ligand binding throughout the simulation.[34–36]

ADME properties were predicted using QikProp (Schrödinger, 2025-1) to evaluate the pharmacokinetic profiles of the compounds. Parameters such as absorption, distribution, metabolism, and excretion were computed, providing a data-driven assessment of drug-likeness and bioavailability.[31]

4. Conclusion

This work demonstrates the successful application of structure-based drug design and molecular hybridization to generate a series of dual-acting hybrid molecules with the potential to address the comorbidity of Alzheimer's disease (AD) and type 2 diabetes mellitus (T2DM). A range of biological activities was observed among the synthesized compounds, with **3d** and **3h** demonstrating selective and potent inhibition of α-Amy and α-Glu, respectively. Similarly, **3i** and **4i** exhibited marked inhibitory effects on ACHE and BCHE. These findings suggest the potential of these molecules as promising scaffolds for developing therapeutics targeting diabetes mellitus and Alzheimer's disease. *In silico* ADME profiling further revealed favorable pharmacokinetic properties consistent with peripheral and central bioavailability, reinforcing their suitability as drug-like candidates. Collectively, these findings position compounds **3d**, **3h**, **3i**, and **4i** as promising lead scaffolds for the development of innovative multi-target therapeutics capable of simultaneously addressing the metabolic and neurodegenerative aspects of AD–T2DM comorbidity. Distinctly, MD simulations confirmed that **4i** forms stable and sustained interactions with its target, further supporting its advancement in preclinical studies. Building on these findings, future work should focus on in-depth mechanistic studies, *in vivo* pharmacokinetic and pharmacodynamic evaluations, and toxicity assessments to validate the safety and efficacy of these hybrid compounds.

Author contributions

Wesam S. Qayed, investigation, conceptualization, supervision, visualization, writing – review & editing, Mostafa A. Hassan methodology, conceptualization, data curation, writing – review & editing, Halil Şenol conceptualization, methodology, software, data curation, visualization, writing – review & editing, Parham Taslimi data curation, methodology, writing – original draft, Tarek Aboul-Fadl, investigation, validation, supervision, writing – review & editing, project administration. All authors reviewed and approved the final manuscript.

Conflicts of interest

There are no conflicts to declare.

Data availability

The data supporting this article have been included as part of the supplementary information (SI).

Supplementary information is available. See DOI: https://doi.org/10.1039/d5md00628g.

References

1 M. Kciuk, W. Kruczkowska, J. Gałęziewska, K. Wanke, Ż. Kałuzińska-Kołat and M. Aleksandrowicz, *et al.*, Alzheimer's Disease as Type 3 Diabetes: Understanding the Link and Implications, *Int. J. Mol. Sci.*, 2024, **25**(22), 11955, DOI: 10.3390/ijms252211955.

2 H. M. Al-Kuraishy, G. M. Sulaiman, H. A. Mohammed, S. G. Mohammed, A. I. Al-Gareeb and A. K. Albuhadily, *et al.*, Amyloid-β and heart failure in Alzheimer's disease: the new vistas, *Front. Med.*, 2025, **12**, 1–12.

3 T. T. Nguyen, Q. T. H. Ta, T. K. O. Nguyen, T. T. D. Nguyen and G. V. Van, Type 3 diabetes and its role implications in alzheimer's disease, *Int. J. Mol. Sci.*, 2020, **21**(9), 1–16.

4 T. Ponce-Lopez, Peripheral Inflammation and Insulin Resistance: Their Impact on Blood–Brain Barrier Integrity and Glia Activation in Alzheimer's Disease, *Int. J. Mol. Sci.*, 2025, **26**(9), 4209, DOI: 10.3390/ijms26094209.

5 R. Nath, S. Pathania, G. Grover and M. J. Akhtar, Isatin containing heterocycles for different biological activities: Analysis of structure activity relationship, *J. Mol. Struct.*, 2020, **1222**, 128900, available from: https://www.sciencedirect.com/science/article/pii/S0022286020312254.

6 B. Mavroidi, A. Kaminari, D. Matiadis, D. Hadjipavlou-Litina, M. Pelecanou and A. Tzinia, *et al.*, The Prophylactic and Multimodal Activity of Two Isatin Thiosemicarbazones against Alzheimer's Disease In Vitro, *Brain Sci.*, 2022, **12**(6), 806, DOI: 10.3390/brainsci12060806.
7 S. Patil, S. G. Alegaon, S. Gharge, S. D. Ranade and N. A. Khatib, Molecular hybridization, synthesis, in vitro α-glucosidase inhibition, in vivo antidiabetic activity and computational studies of isatin based compounds, *Bioorg. Chem.*, 2024, **153**, 107783, DOI: 10.1016/j.bioorg.2024.107783.
8 Z. Bakherad, H. Bakherad, S. Sepehri, M. A. Faramarzi, K. Mahnam and S. Mojtabavi, *et al.*, In silico and in vitro studies of thiosemicarbazone-indole hybrid compounds as potent α-glycosidase inhibitors, *Comput. Biol. Chem.*, 2022, **97**, 107642, DOI: 10.1016/j.compbiolchem.2022.107642.
9 A. Y. Alzahrani, Y. A. Ammar, M. Abu-Elghait, M. A. Salem, M. A. Assiri and T. E. Ali, *et al.*, Development of novel indolin-2-one derivative incorporating thiazole moiety as DHFR and quorum sensing inhibitors: synthesis, antimicrobial, and antibiofilm activities with molecular modelling study, *Bioorg. Chem.*, 2021, **119**, 105571, DOI: 10.1016/j.bioorg.2021.105571.
10 H. E. Lebovitz, Differentiating members of the thiazolidinedione class: a focus on safety, *Diabetes/Metab. Res. Rev.*, 2002, **18**(S2), S23–S29, DOI: 10.1002/dmrr.252.
11 M. Michailidis, D. A. Tata, D. Moraitou, D. Kavvadas, S. Karachrysafi and T. Papamitsou, *et al.*, Antidiabetic Drugs in the Treatment of Alzheimer's Disease, *Int. J. Mol. Sci.*, 2022, **23**(9), 4641, DOI: 10.3390/ijms23094641.
12 W. S. Qayed, M. A. Hassan, A. M. Abouwarda, Y. M. Ibrahim and T. Aboul-Fadl, Computational Design of Azine-Linked Hybrids of 2-Indolinone-Thiazolodine Scaffold as Novel and Promising Quorum Sensing Inhibitors, *Polycyclic Aromat. Compd.*, 2024, **44**(1), 1–24, DOI: 10.1080/10406638.2023.2165511.
13 W. S. Qayed, M. A. Hassan, W. M. El-Sayed, A. S. Rogério and T. Aboul-Fadl, Novel Azine Linked Hybrids of 2-Indolinoneand ThiazolodinoneScaffolds as CDK2 Inhibitors with Potential Anticancer Activity: In Silico Design, Synthesis, Biological, Molecular Dynamics and Binding Free Energy Studies, *Bioorg. Chem.*, 2022, **126**, 104366, DOI: 10.1016/j.bioorg.2020.10436.
14 B. D. Varpe, A. A. Kulkarni, S. B. Jadhav, A. S. M. Jadhav and S. Y. Jadhav, Isatin Hybrids and Their Pharmacological Investigations, *Mini-Rev. Med. Chem.*, 2021, **21**, 1182–1225, available from: http://www.eurekaselect.com/node/188949/article.
15 H. Yakan, M. Azam, S. Kansız, H. Muğlu, M. Ergül, P. Taslimi, Ü. M. Koçyiğit, M. Karaman, A. Siar and K. Min, Evaluation as anti-proliferative agents and metabolic enzyme, *Bull. Chem. Soc. Ethiop.*, 2023, **37**(5), 1221–1236.
16 X. Gong, S. Li, J. Huang, S. Tan, Q. Zhang and Y. Tian, *et al.*, Discovery of potent LRRK2 inhibitors by ensemble virtual screening strategy and bioactivity evaluation, *Eur. J. Med. Chem.*, 2024, **279**, 116812, DOI: 10.1016/j.ejmech.2024.116812.
17 H. El-Kashef, G. Badr, N. Abo El-Maali, D. Sayed, P. Melnyk and N. Lebegue, *et al.*, Synthesis of a novel series of (Z)-3,5-disubstituted thiazolidine-2,4-diones as promising anti-breast cancer agents, *Bioorg. Chem.*, 2020, **96**, 103569, DOI: 10.1016/j.bioorg.2020.103569.
18 A. Stana, B. Tiperciuc, M. Duma, L. Vlase, O. Crișan and A. Pîrnău, *et al.*, Synthesis and Antimicrobial Activity of Some New N-substituted-5-arylidene-thiazolidine-2,4-diones, *J. Heterocyclic Chem.*, 2014, **51**(2), 411–417, DOI: 10.1002/jhet.1726.
19 G. L. Ellman, K. D. Courtney, V. Andres and R. M. Featherstone, A new and rapid colorimetric determination of acetylcholinesterase activity, *Biochem. Pharmacol.*, 1961, **7**(2), 88–95, DOI: 10.1016/0006-2952(61)90145-9.
20 L. Durmaz, H. Karageçili, A. Erturk, E. M. Ozden, P. Taslimi and S. Alwasel, *et al.*, Hamamelitannin's Antioxidant Effect and Its Inhibition Capability on α-Glycosidase, Carbonic Anhydrase, Acetylcholinesterase, and Butyrylcholinesterase Enzymes, *Processes*, 2024, **12**(11), 2341, DOI: 10.3390/pr12112341.
21 H. Yalazan, D. Koç, F. Aydın Kose, S. Fandaklı, B. Tüzün and M. İ. Akgül, *et al.*, Design, syntheses, theoretical calculations, MM-GBSA, potential anti-cancer and enzyme activities of novel Schiff base compounds, *J. Biomol. Struct. Dyn.*, 2023, **42**(23), 13100–13113, DOI: 10.1080/07391102.2023.2274972.
22 S. Zareei, M. Mohammadi-Khanaposhtani, M. Shahali, H. Şenol, M. Badbedast and A. Moazzam, *et al.*, Phenyldiazenyl-phenoxy-1,2,3-triazol-acetamide derivatives as new dual cholinesterase Inhibitors: Design, synthesis, in vitro, and in silico enzymatic inhibition evaluations, *J. Mol. Struct.*, 2025, **1321**, 139686, DOI: 10.1016/j.molstruc.2024.139686.
23 Y. Tao, Y. Zhang, Y. Cheng and Y. Wang, Rapid screening and identification of α-glucosidase inhibitors from mulberry leaves using enzyme-immobilized magnetic beads coupled with HPLC/MS and NMR, *Biomed. Chromatogr.*, 2012, **27**(2), 148–155, DOI: 10.1002/bmc.2761.
24 Z. Xiao, R. Storms and A. Tsang, A quantitative starch–iodine method for measuring alpha-amylase and glucoamylase activities, *Anal. Biochem.*, 2006, **351**(1), 146–148, DOI: 10.1016/j.ab.2006.01.036.
25 M. H. Sayahi, S. Zareei, M. Halimi, M. Alikhani, A. Moazzam and M. Mohammadi-Khanaposhtani, *et al.*, Design, synthesis, in vitro, and in silico anti-α-glucosidase assays of N-phenylacetamide-1,2,3-triazole-indole-2-carboxamide derivatives as new anti-diabetic agents, *Sci. Rep.*, 2024, **14**(1), 15791, Available from: https://pubmed.ncbi.nlm.nih.gov/38982268.
26 R. D. Alharthy, S. Khalid, S. Fatima, S. Ullah, A. Khan and S. N. Mali, *et al.*, Synthesis of the chromone-thiosemicarbazone scaffold as promising α-glucosidase inhibitors: An in vitro and in silico approach toward antidiabetic drug design, *Arch. Pharm.*, 2024, **357**(8), 2400140, DOI: 10.1002/ardp.202400140.
27 M. B. Haider, A. Saeed, A. Ahmed, M. Azeem, H. Ismail and S. Mehmood, *et al.*, Exploring Acyl Thiotriazinoindole Based Pharmacophores: Design, Synthesis, and SAR Studies with Molecular Docking and Biological Activity Profiling against Urease, α-amylase, α-glucosidase, Antimicrobial, and Antioxidant Targets, *Protein J.*, 2024, **43**(5), 1009–1024, DOI: 10.1007/s10930-024-10229-6.

28 F. S. Tokalı, H. Şenol, Ş. Ateşoğlu, P. Tokalı and F. Akbaş, Exploring highly selective polymethoxy fenamate isosteres as novel anti-prostate cancer agents: Synthesis, biological activity, molecular docking, molecular dynamics, and ADME studies, *J. Mol. Struct.*, 2025, **1319**, 139519, DOI: 10.1016/j.molstruc.2024.139519.

29 I. Mamedov, H. Şenol, F. Naghiyev, V. Khrustalev, N. Sadeghian and P. Taslimi, New tetrahydro-isoquinoline derivatives as cholinesterase and α-glycosidase inhibitors: Synthesis, characterization, molecular docking & dynamics, ADME prediction, in vitro cytotoxicity and enzyme inhibition studies, *J. Mol. Liq.*, 2024, **404**, 125006, DOI: 10.1016/j.molliq.2024.125006.

30 H. Şenol, 4-Furfuryloxymethyl-1,2,3-triazol-1-yl-acetohydrazide Hybrids as Cholinesterase and Carbonic Anhydrase Inhibitors: Synthesis, Characterization and Comprehensive Biological Activity Studies, *ChemistrySelect*, 2024, **9**(6), 202303927, DOI: 10.1002/slct.202303927.

31 N. Kılınç, Inhibition profiles and molecular docking studies of antiproliferative agents against aldose reductase enzyme, *Int. J. Chem. Technol.*, 2021, **5**(1), 77–82, DOI: 10.32571/ijct.944049.

32 F. S. Tokalı, H. Şenol, Ş. Ateşoğlu and F. Akbaş, A series of quinazolin-4(3H)-one-morpholine hybrids as anti-lung-cancer agents: Synthesis, molecular docking, molecular dynamics, ADME prediction and biological activity studies, *Chem. Biol. Drug Des.*, 2024, **104**(1), 14599, DOI: 10.1111/cbdd.14599.

33 K. B. Zengin, D. Öztürk Civelek, E. B. Çakmak, Y. Kolcuoğlu, H. Şenol and B. N. Sağlık Özkan, *et al.*, Synthesis of Sorafenib-Ruthenium Complexes, Investigation of Biological Activities and Applications in Drug Delivery Systems as an Anticancer Agent, *J. Med. Chem.*, 2024, **67**(6), 4463–4482, Available from: https://pubmed.ncbi.nlm.nih.gov/38471014.

34 Z. Arslan, E. Okuroğlu, H. Şenol and Z. Türkmen, 1-Benzhydryl-piperazine: Isolation, structure determination, and in silico studies for a novel potential narcotic agent detected in sports supplements, *J. Food Compos. Anal.*, 2024, **135**, 106682, DOI: 10.1016/j.jfca.2024.106682.

35 E. Hacıosmanoğlu-Aldoğan, D. Lama, H. İ. Yetke, H. Şenol and F. D. Yöntem, Necroptotic Suppression of Lung Cancer Cell Proliferation and Migration: A Comprehensive In Vitro and In Silico Study to Determine New Molecular Targets for Pexidartinib, *Cell Biochem. Funct.*, 2025, **43**(3), 70068, DOI: 10.1002/cbf.70068.

36 F. Çakır, Ş. Ateşoğlu, Z. R. Müderrisoğlu, F. Demirel, F. Akbaş and F. S. Tokalı, *et al.*, Targeting Lung Cancer With Carvacrol-Triazole-Arylidene Hydrazide Hybrids: In Vitro and In Silico Cytotoxicity Assessments, *Chem. Biodiversity*, 2025, 2963, DOI: 10.1002/cbdv.202402963.

